

Whistler emission in the separatrix regions of asymmetric magnetic reconnection

D. B. Graham¹, A. Vaivads¹, Yu. V. Khotyaintsev¹, and M. André¹

An edited version of this paper was published by AGU. Copyright (2016) American Geophysical Union. Graham, D. B., A. Vaivads, Y. V. Khotyaintsev, and M. André (2016), Whistler emission in the separatrix regions of asymmetric magnetic reconnection, *J. Geophys. Res. Space Physics*, 121, 1934-1954, doi:10.1002/2015JA021239. To view the published open abstract, go to <http://dx.doi.org> and enter the DOI.

¹Swedish Institute of Space Physics,

Uppsala, Sweden.

Abstract. At Earth's dayside magnetopause asymmetric magnetic reconnection occurs between the cold dense magnetosheath plasma and the hot tenuous magnetospheric plasma, which differs significantly from symmetric reconnection. During magnetic reconnection the separatrix regions are potentially unstable to a variety of instabilities. In this paper observations of the separatrix regions of asymmetric reconnection are reported as Cluster crossed the magnetopause near the subsolar point. The small relative motion between the spacecraft and plasma allows spatial changes of electron distributions within the separatrix regions to be resolved over multiple spacecraft spins. The electron distributions are shown to be unstable to the electromagnetic whistler mode and the electrostatic beam mode. Large-amplitude whistler waves are observed in the magnetospheric and magnetosheath separatrix regions, and outflow region. In the magnetospheric separatrix regions the observed whistler waves propagate toward the X line, which are shown to be driven by the loss in magnetospheric electrons propagating away from the X line, and are enhanced by the presence of magnetosheath electrons. The beam mode waves are predicted to be produced by beams of magnetosheath electrons propagating away from the X line, and potentially account for some of the electrostatic fluctuations observed in the magnetospheric separatrix regions.

1. Introduction

Magnetic reconnection occurs when two plasmas with different magnetic field topologies interact to change the magnetic field structure. Magnetic reconnection transforms magnetic field energy into particle kinetic energy in the form of acceleration and heating. Magnetic reconnection is well known to occur at Earth's magnetopause [Sonnerup *et al.*, 1981; Paschmann *et al.*, 1982; Gosling *et al.*, 1982] and magnetotail [Øieroset *et al.*, 2001], and is responsible for solar particles entering Earth's magnetosphere. The magnetic field lines reconnect in a small region called the diffusion region, where the frozen-in condition of ions then electrons is violated and magnetic fields "reconnect" [Priest and Forbes, 2000]. Although the diffusion region is small, magnetic reconnection leads to large-scale changes in the plasmas. For example, the ion outflows reach high speeds outside the diffusion region and extend large distances away from the diffusion region.

Spacecraft observations and simulations have primarily focused on symmetric reconnection, in which the reconnecting plasmas have the same properties and magnetic field strength. As a result, symmetric reconnection is generally well understood [Birn *et al.*, 2001; Øieroset *et al.*, 2001; Mozer *et al.*, 2002]. In contrast, asymmetric reconnection, in which the plasmas have different properties, is not well understood. Simulations and observations show that asymmetric reconnection differs significantly from symmetric reconnection [Swisdak *et al.*, 2003; Mozer *et al.*, 2008; Pritchett, 2008; Tanaka *et al.*, 2008; Graham *et al.*, 2014]. In particular, at Earth's dayside magnetopause the electron density and temperature of the reconnecting plasmas often differ by over an order of magnitude, which leads to different electron distributions associated with magnetic reconnection

[*Graham et al.*, 2014]. Therefore, the instabilities in the separatrix regions of asymmetric reconnection may differ significantly from those found in symmetric reconnection, for example, at Earth's magnetotail.

The separatrix regions bound the inflowing and outflowing plasmas associated with reconnection. They have been observed to extend large distances from the diffusion region [André *et al.*, 2004; Khotyaintsev *et al.*, 2006]. The separatrix regions of symmetric and asymmetric magnetic reconnection are characterized by anisotropic electron distributions [Gosling *et al.*, 1990; André *et al.*, 2010], strong parallel currents [André *et al.*, 2004; Khotyaintsev *et al.*, 2006; Wang *et al.*, 2012], and increased electric field activity [Retinò *et al.*, 2006; Lindstedt *et al.*, 2009; Viberg *et al.*, 2013; Wang *et al.*, 2013]. A variety of wave modes have been reported in the separatrix regions of symmetric reconnection, for example, electrostatic solitary waves (ESWs) [Cattell *et al.*, 2005; Fujimoto *et al.*, 2011], double layers [Wang *et al.*, 2014], Langmuir waves [Farrell *et al.*, 2002], lower-hybrid waves [Zhou *et al.*, 2009], electron cyclotron harmonic waves [Viberg *et al.*, 2013], whistler waves [Deng *et al.*, 2004], and kinetic Alfvén waves [Chaston *et al.*, 2005]. Simulations likewise show that multiple wave modes can develop in the separatrix regions [Goldman *et al.*, 2008; Divin *et al.*, 2012; Fujimoto, 2014]. However, for asymmetric reconnection at the magnetopause the electron distributions in the separatrix regions differ from those associated with symmetric reconnection. In particular, anisotropic electron distributions result from magnetosheath electrons entering the magnetosphere along reconnected field lines and escaping magnetospheric electrons, which have distinct temperatures [André *et al.*, 2010].

One of the waves frequently observed with magnetic reconnection at the magnetopause and magnetotail is the whistler wave [Gurnett *et al.*, 1976; Zhang *et al.*, 1999; Deng and Matsumoto, 2001; Petkaki *et al.*, 2006; Wei *et al.*, 2007; Tang *et al.*, 2013]. In Earth's magnetotail whistler emission is associated with increased electron fluxes parallel to \mathbf{B} and field-aligned currents [Gurnett *et al.*, 1976; Wei *et al.*, 2007; Teste and Parks, 2009], and is argued to be generated by electron beams [Zhang *et al.*, 1999]. At the magnetopause whistler emission is observed in thin current sheets, which are argued to be connected to the magnetic reconnection site [Stenberg *et al.*, 2005, 2007], and near the electron diffusion region [Tang *et al.*, 2013]. These whistler waves are consistent with generation by the temperature anisotropy of the magnetospheric electron population [Stenberg *et al.*, 2005; Vaivads *et al.*, 2007]. Whistler waves are also associated with dipolarization fronts in the magnetotail [Viberg *et al.*, 2014], and occur in the form of chorus emission in the magnetosphere [Santolík *et al.*, 2004, 2014]. Whistler waves are electromagnetic right-hand circularly polarized waves with frequencies between the lower-hybrid frequency f_{LH} and the electron cyclotron frequency f_{ce} . Whistler waves are known to be generated by temperature anisotropies [Kennel and Petschek, 1966], but can also be generated by electron beams [Bell and Buneman, 1964] and heat flux instabilities [Gary *et al.*, 1994]. Recently, Goldman *et al.* [2014] showed that whistler waves can be generated by Čerenkov emission from ESWs. It is therefore of interest to characterize the observed whistler waves, investigate how they are generated, and their effects on magnetic reconnection.

In this paper we report observations of the electron distributions and wave activity in the magnetospheric and magnetosheath separatrix regions of asymmetric magnetic reconnection. The electron distributions in the magnetospheric separatrix regions become

unstable due to a partial loss in magnetospheric electrons and beams of magnetosheath electrons, which produce loss-cone distributions. The partial loss in magnetospheric electrons is shown to generate whistler waves, while the beams are predicted to excite the electrostatic beam mode, potentially generating broadband electrostatic fluctuations. The electron distributions in the magnetosheath separatrix regions are anisotropic due to escaping magnetospheric electrons. The magnetosheath separatrix regions are likewise shown to excite electromagnetic whistler waves. In the magnetospheric separatrix regions the whistler waves propagate toward the X line, whereas in the magnetosheath separatrix regions the whistler waves are predicted to propagate away from the X line. The origin of the unstable electron distributions is discussed, as well as the possible effects of the waves on asymmetric reconnection.

The outline of this paper is as follows. In section 2 we state the instruments and data used. Sections 3 and 4 present case studies of separatrix regions observed on 17 April 2007 and 22 April 2008, respectively. Section 5 is the discussion and in section 6 the conclusions are stated.

2. Instruments and Data

To investigate the separatrix regions we use data from the Cluster spacecraft. We use electron data from the Plasma Electron and Current Experiment (PEACE), magnetic field **B** data from the Fluxgate Magnetometer (FGM), electric field data from the Electric Field and Wave experiment (EFW), and electric and magnetic field spectral data from the Spatio-Temporal Analysis of Field Fluctuation experiment (STAFF) [Escoubet *et al.*, 2001]. The electric fields from EFW and STAFF are only recorded in the spacecraft spin plane, corresponding roughly to the Geocentric Solar Ecliptic (GSE) x and y directions.

For the events investigated in this paper all instruments were operating in spacecraft burst mode, with higher time resolution data. In particular, PEACE performs energy sweeps at 8 Hz, although ~ 2 s (half the spacecraft spin period) is required to obtain a full pitch-angle distribution. The spectral power densities of the electric field \mathbf{E} and magnetic field \mathbf{B} are recorded by STAFF at 8 Hz, and the polarization and propagation parameters are recorded at 1 Hz.

The magnetopause crossings we investigate were observed on 17 April 2007 and 22 April 2008 during the outward bound portion of the orbit. Figures 1a–1b and 1h–1i show the spacecraft separations at the time of the magnetopause crossing for the two events, presented in Geocentric Solar Magnetospheric (GSM) coordinates. Cluster 1 (C1), Cluster 2 (C2), and Cluster 3 (C3) are well separated from each other, while Cluster 4 (C4) is close to C3. The spacecraft are separated by ~ 1 Earth radius (R_E) in the Y and Z directions, but have relatively small separations in the X direction (the maximum separation in the X direction is $\sim 0.4 R_E$ between C1 and C2), meaning the spacecraft crossed the magnetopause at similar times. For both events C1 and C2 are located about $1 R_E$ northward of C3 and C4 (Figures 1b and 1i).

For both events C2 crossed the magnetopause northward of the X line, confirmed by the northward ion outflows observed by C1 and C3, shown in Figure 1. The maximum observed ion outflow speeds are $\sim 400 \text{ km s}^{-1}$ and 330 km s^{-1} for the 17 April 2007 and 22 April 2008 events, respectively. From the magnetospheric and magnetosheath properties we estimate the density of the outflow regions to be $n_{\text{out}} \sim (n_{\text{MS}} B_{\text{SH}} + n_{\text{SH}} B_{\text{MS}}) / (B_{\text{MS}} + B_{\text{SH}}) \sim 8 \text{ cm}^{-3}$ and $\sim 13 \text{ cm}^{-3}$ on 17 April 2007 and 22 April 2008, respectively, based on the scalings in *Cassak and Shay* [2007]. The outflow speeds are predicted to be $v_{\text{out}} \sim$

$\sqrt{B_{\text{MS}}B_{\text{SH}}/(\mu_0 m_i n_{\text{out}})} \sim 400 \text{ km s}^{-1}$ and $\sim 300 \text{ km s}^{-1}$ on 17 April 2007 and 22 April 2008, respectively [Cassak and Shay, 2007]. These values agree with the maximum northward outflow speeds observed in Figure 1, consistent with the spacecraft crossing the ion outflow regions north of the X line. On 22 April 2008 the maximum outflow speeds are smaller because n_{SH} is larger, which decreases the ion Alfvén speed. The maximum outflows speeds tend to be observed when $B_z > 0$, i.e., on the magnetospheric side of the current sheet. This is consistent with simulations of magnetic reconnection with a large density asymmetry, where the ion outflow regions tend to shift toward the lower density side of the current sheet [Pritchett, 2008; Tanaka et al., 2008]. In the following sections we present detailed observations of the two events using C2, analyze the electron distributions in the magnetospheric and magnetosheath separatrix regions, and investigate the associated instabilities.

Table 1 shows the ratios of magnetospheric to magnetosheath $|\mathbf{B}|$, $B_{\text{MS}}/B_{\text{SH}}$, electron number density $n_{\text{MS}}/n_{\text{SH}}$, and electron temperature $T_{e\text{MS}}/T_{e\text{SH}}$. Both reconnection events are qualitatively similar. Both events have comparable B_{MS} and B_{SH} . However, the electron number densities n_e and electron temperatures T_e of the reconnecting plasmas differ by over an order of magnitude, making reconnection highly asymmetric. The shear angles θ_s between \mathbf{B}_{MS} and \mathbf{B}_{SH} are large, corresponding to weak guide-field reconnection. At the time of the magnetopause crossings \mathbf{B}_{SH} was southward, consistent with asymmetric reconnection occurring near the subsolar point. Here, θ_s is calculated from C2 when C2 was in the magnetosphere and magnetosheath, at times close to the magnetopause crossing. Therefore, there is some uncertainty in θ_s because \mathbf{B}_{MS} and \mathbf{B}_{SH} cannot be measured

simultaneously. Similarly, C2 was outside the diffusion region, so θ_s may differ closer to the diffusion region.

3. 17 April 2007

3.1. Overview

On 17 April 2007 we investigate a time interval containing two crossings of the magnetospheric separatrix regions observed by C2. We define the magnetospheric separatrix regions to be the regions that bound the ion outflow region and the first reconnected magnetospheric field lines [Lindstedt *et al.*, 2009]. The reconnected field lines are identified by the presence of magnetosheath electrons entering the magnetosphere. Figure 2 presents an overview of the event. At this time C2 was located at $(8.7, -4.9, 2.6)R_E$ (GSM). C2 began in the ion outflow region, characterized by high n_e compared with the magnetospheric n_e (Figure 2c) and mixing of magnetospheric and magnetosheath electrons, as indicated by the electron differential energy fluxes, shown in Figure 2b. The electron differential energy fluxes are presented at subspin resolution. C2 entered the magnetospheric separatrix region and then entered the magnetosphere, characterized by low-density high-temperature electrons, and negligible fluxes of cold electrons. C2 was in the magnetosphere between 15:33:47 UT and 15:34:15 UT. For this event $T_{eMS} \approx 1700$ eV and $T_{eSH} \approx 35$ eV, so the magnetospheric and magnetosheath electron populations are easily distinguished. C2 then entered the magnetospheric separatrix region and the ion outflow region. Throughout the magnetospheric separatrix regions \mathbf{B} remains northward, corresponding to the magnetospheric side of the magnetopause. Figure 2c indicates the times when C2 was in the ion outflow regions, magnetospheric and magnetosheath separatrix regions, and the magnetosphere.

After $\sim 15:37:15$ UT vertical striations are observed in the electron differential energy flux. These striations correspond to the spacecraft spin when the electron distribution becomes anisotropic. In particular, the electrons at higher energies primarily propagate antiparallel to \mathbf{B} (found by inspection of the electron pitch-angle distributions and discussed in the following subsection). This indicates that the magnetospheric electrons have not been significantly scattered in pitch angle and correspond to electrons following reconnected field lines away from the X line. In contrast, prior to $\sim 15:37:15$ UT, the vertical striations associated with the spacecraft spin are small, corresponding to more isotropic electron distributions. The development of these striations indicates that the electron distributions change, suggesting C2 has entered a different reconnection region. Our interpretation is that at $\sim 15:37:15$ UT C2 moved from the outflow region into the magnetosheath separatrix region, where electrons exiting the magnetosphere along reconnected field lines have not been significantly scattered in pitch angle. At this time \mathbf{B} is typically southward and is similar to the magnetosheath \mathbf{B} . This region bounds the outflow region and the magnetosheath.

We calculate the $\mathbf{E} \times \mathbf{B}$ drift velocity \mathbf{V}_E because ion data are unavailable on C2. We assume $\mathbf{E} \cdot \mathbf{B} = 0$ to estimate \mathbf{E} along the spacecraft spin axis and calculate \mathbf{V}_E in three dimensions. We remove the points when \mathbf{B} is close to the spacecraft spin plane because the estimates of \mathbf{E} along the spacecraft spin axis become unreliable. Figure 2d shows that \mathbf{V}_E has a northward flow throughout most of the region, with components in the negative x- and y-directions. The difference in direction between \mathbf{V}_E and the ion outflows observed in Figure 1, which are primarily northward, may be because \mathbf{V}_E does not include motion parallel to \mathbf{B} . The flows are observed at the same times as the mixing

of the magnetospheric and magnetosheath electrons, consistent with reconnection outflow regions. In the unperturbed magnetosphere \mathbf{V}_E is negligible. We note that large \mathbf{V}_E are also observed in the separatrix regions. However, these regions are not ion outflow regions because n_e is too small. Both C1 and C3 observed northward ion outflows, confirming that C2 crossed the magnetopause north of the diffusion region. In general, \mathbf{V}_E is smaller than the ion outflows measured by C1 and C3 and can differ in direction because \mathbf{V}_E neglects ion velocity parallel to \mathbf{B} . In particular, the z-component of \mathbf{V}_E is significantly smaller than \mathbf{V} obtained from the ion moments.

In the magnetospheric separatrix regions cold magnetosheath electrons are observed, but have densities well below those observed in the outflow region. The density of magnetospheric electrons is below the unperturbed magnetosphere, indicated by the decrease in the differential energy fluxes above 1 keV in Figure 2b. This means there is a partial loss in magnetospheric electrons associated with the reconnected \mathbf{B} . However, n_e typically remains comparable to the magnetospheric n_e based on the electron moments (Figure 2c), meaning the density of magnetosheath electrons is comparable to the loss in magnetospheric electrons. As a result, the magnetospheric separatrix regions have T_e between the magnetospheric and outflow T_e . For the separatrix region between 15:33:17 UT and 15:33:47 UT the density of magnetosheath electrons decreases, while the density of magnetospheric electrons increases. This results in T_e increasing by over an order of magnitude as C2 crossed the from the outflow region to the magnetosphere, as seen in Figure 2b. The electron density inferred from the spacecraft potential shows that density cavities coincide with the magnetospheric separatrix regions, consistent with previous observations [Khotyaintsev *et al.*, 2006; Lindstedt *et al.*, 2009; André *et al.*, 2010]. However,

the large changes in T_e within these regions makes the inferred density from the spacecraft potential unreliable.

The magnetospheric separatrix regions show increased wave activity. Figures 2e and 2f show the spectrograms of **E** and **B** from STAFF. (The gaps in the **E** spectrogram occur when WHISPER is in sounding mode.) The spectrogram of **E** shows broadband emissions, which are typically most intense below $0.1f_{ce}$, but can extend above f_{ce} , where f_{ce} is the electron cyclotron frequency. More narrowband emission is also observed near $0.5f_{ce}$. The spectrogram of **B** also shows intense emission near $0.5f_{ce}$, indicating that these waves are electromagnetic. Figure 2h shows the ellipticity with respect to the background magnetic field direction. For the observed electromagnetic waves the ellipticity is +1, indicating right-hand circular polarization. Therefore, we identify the waves as electromagnetic whistler waves. By comparing Figures 2e–2f with Figure 2b we see that these whistlers tend to be localized to the magnetospheric separatrix regions, where magnetospheric and magnetosheath electrons are observed and n_e is small. In the unperturbed magnetosphere negligible whistler emission is observed.

Whistler emission is also observed in the outflow region and magnetosheath separatrices. In these regions whistler emission is intermittent and typically has frequencies $f < 0.5f_{ce}$, although some whistler emission is observed at $\sim 15:38:15$ UT with $f > 0.5f_{ce}$. Some of the whistler emission is correlated with local decreases in **B**, indicated by the decrease in f_{ce} , similar to magnetosheath lion roars [Baumjohann *et al.*, 1999]. However, some regions of whistler emission, for instance the green shaded interval in Figure 2, show no significant changes in the magnitude of **B**, meaning these whistlers are not generated by electron trapping associated with changes in **B**, as typically expected for lion roars. Over

the entire region in Figure 2, the wave normal angle θ_k associated with the whistler waves (not shown) typically remains close to 0° , corresponding to wave propagation close to parallel (or antiparallel) to \mathbf{B} .

To estimate the phase speed v_{ph} of the whistler waves we plot $|\mathbf{E}|/|\mathbf{B}|$ in Figure 2g. We note that \mathbf{E} only includes the field in the spacecraft spin plane, so the power of \mathbf{E} is likely underestimated. Additionally, some broadband electrostatic fluctuations reach f_{ce} , so there is some uncertainty in v_{ph} . We estimate v_{ph} for the whistlers by averaging $|\mathbf{E}|/|\mathbf{B}|$ over the time intervals when whistlers are observed for the frequency f_{\max} where the power is maximal. For the blue and red shaded intervals in Figure 2, corresponding to times within the magnetospheric separatrix regions, we estimate $v_{ph} = 4.3 \times 10^4 \text{ km s}^{-1}$ and $2.0 \times 10^4 \text{ km s}^{-1}$, respectively. We calculate the parallel wavelengths λ_{\parallel} of the whistler waves to be $\lambda_{\parallel} = v_{ph}/f_{\max} = 54 \text{ km}$ and 25 km for the blue and red intervals, respectively. These estimates are consistent with previous observations at the magnetopause [Stenberg *et al.*, 2005; Vaivads *et al.*, 2007]. From the gyroresonance condition, the speed of the resonant electrons is $v_{\parallel\text{res}} = (f - f_{ce})\lambda_{\parallel}$ [Kennel and Petschek, 1966; Vaivads *et al.*, 2007]. Based on the above estimates we calculate $v_{\parallel\text{res}} = 3.2 \times 10^4 \text{ km s}^{-1}$ and $1.3 \times 10^4 \text{ km s}^{-1}$, or equivalently 3 keV and 500 eV . Therefore, in the magnetospheric separatrix regions the resonant electrons are associated with the magnetospheric plasma.

Qualitatively, the whistlers observed in the outflow region and magnetosheath separatrix regions differ from the whistlers in the magnetospheric separatrix regions. In particular, in the magnetospheric separatrix regions $f \gtrsim 0.5f_{ce}$, whereas in the ion outflow regions and magnetosheath separatrix regions f is typically less than $0.5f_{ce}$ and the whistlers have smaller v_{ph} . As an example we investigate in detail the green shaded interval in Figure

2, which likely corresponds to a time of whistler emission in the magnetosheath separatrix region. At this time \mathbf{V}_E is small and the electron distributions become anisotropic, suggesting that C2 was outside the ion outflow region. For the whistlers observed at this time we estimate $v_{ph} = 5.1 \times 10^3 \text{ km s}^{-1}$ and $\lambda_{\parallel} = 15 \text{ km}$, which are smaller than those of the whistlers in magnetospheric separatrix regions. The approximate resonant speed is $v_{\parallel\text{res}} = 1.4 \times 10^4 \text{ km s}^{-1}$, or equivalently 600 eV, over an order of magnitude larger than $T_{e\text{SH}}$. This indicates that the resonant electrons are magnetospheric or accelerated magnetosheath electrons, even though the electron distribution is dominated by cold magnetosheath electrons.

The parallel Poynting vector normalized by its standard deviation is plotted in Figure 2i. For the whistlers in the magnetospheric separatrix regions the direction of the Poynting vector is antiparallel to \mathbf{B} , meaning the whistlers propagate toward the X line. In the ion outflow region and magnetosheath separatrix regions the parallel Poynting vector remains close to 0, so the propagation direction is unclear.

For the whistler waves observed in the blue shaded region of Figure 2 EFW's internal burst mode was triggered, recording the electric field at 9000 samples/s. The time series of \mathbf{E} and the associated wavelet spectrogram are plotted in Figures 3a and 3b. The field is displayed in spacecraft coordinates, approximately corresponding to the GSE x and y directions. The whistler waves are intense, reaching field strengths of $\sim 16 \text{ mV m}^{-1}$. We also briefly observe whistler emission near $0.1f_{ce}$ at 15:33:42 UT. A shorter time series in Figure 3c shows that the whistler waves are composed of wave packets with time scales of $\sim 5 - 10 \text{ ms}$. The packets typically consist of $\lesssim 10$ wave periods, as seen in Figure 3d. The packet time scales and amplitude show significant variations, but are not discrete.

This packet structure is similar to chorus emission [*Santolík et al.*, 2004, 2014]. However, the packet structure may also be consistent with linear growth over a range of wave numbers and frequencies, producing a broad spectral peak. Similar waveforms are found for synthetic data when there is a single broad spectral peak. From Figures 3c and 3d the packets associated with E_x and E_y differ. At this time $\mathbf{B} = (-11.7, 41.5, 24.4)$ nT in spacecraft coordinates, so E_x is primarily in the direction perpendicular to \mathbf{B} and E_y is more closely aligned with \mathbf{B} . The amplitudes of E_x and E_y are comparable and often differ in structure, suggesting that the whistlers are slightly oblique or the electric field has a component aligned with \mathbf{B} . Over this period the range of θ_k (not shown) is $0^\circ \lesssim \theta_k \lesssim 40^\circ$; so the whistlers may be slightly oblique, which may result in a small component of \mathbf{E} aligned with \mathbf{B} . Based on the Fourier transform of the entire waveform in Figure 3e the power is maximal at $0.57f_{ce}$ and ranges from $0.40f_{ce}$ to $0.70f_{ce}$, where $f_{ce} = 1.4$ kHz. Both E_x and E_y have comparable powers at the whistler frequencies. We conclude that the waveform structure may develop from linear growth over a range of frequencies, although we cannot exclude that nonlinear processes contributing to the structure of the waveform are also occurring.

3.2. Electron Distributions and Whistler Waves

In this subsection we investigate the electron distributions produced in the separatrix regions. The electron phase-space densities $f_e(E)$ are obtained at all pitch angles θ by averaging the data over half a spacecraft spin period (~ 2 s). Here, E is the electron energy. Data from PEACE's Low Energy Electron Analyser (LEEA) and High Energy Electron Analyser (HEEA) are combined to cover the energy range $7\text{ eV} < E < 23\text{ keV}$, for both reconnection events. The values of E are corrected for the spacecraft potential

V_{sc} and energy levels saturated by photoelectrons (typically below ~ 10 eV) are removed. We then find fits to the observed electron distributions and investigate the waves modes excited in the separatrix regions.

The electron distributions observed in the separatrix regions, corresponding to the blue, red, and green shaded regions in Figure 2, are shown in Figure 4. We note that $f_e(E)$ changes over the shaded intervals, so the distributions in Figure 4 correspond to times when the anisotropy in the magnetospheric electrons is maximal, indicated by the vertical dashed lines in Figure 2b. Figures 4a–4b and 4d–4e show $f_e(E)$ in the magnetospheric separatrix regions. In Figures 4a–4b there is a small increase in magnetosheath electrons with $E \lesssim 500$ eV near $\theta = 0^\circ$ and 180° . For $E \gtrsim 500$ eV, corresponding to magnetospheric electrons, there is a significant loss in electrons near $\theta = 0^\circ$, which produces a loss-cone distribution at magnetospheric energies. Figures 4d–4e show the same qualitative features for $E \gtrsim 500$ eV, but at low E an intense beam of magnetosheath electrons aligned with \mathbf{B} is observed at $E \approx 100$ eV, corresponding to magnetosheath electrons propagating away from the X line. These electron beams are frequently observed in the magnetospheric separatrix regions.

Figures 4g–4h show $f_e(E)$ in the magnetosheath separatrix region during the green shaded region in Figure 2. The distribution is dominated by magnetosheath electrons, although high-energy magnetospheric electrons remain well above the instrumental one-count level. For $E \gtrsim 100$ eV, $f_e(E)$ at $\theta = 0^\circ$ is significantly below $f_e(E)$ at $\theta = 90^\circ$ and 180° . The enhancement in $f_e(E)$ for $\theta \gtrsim 90^\circ$ is due to accelerated magnetosheath electrons and magnetospheric electrons following the reconnected field lines from the magnetosphere to the magnetosheath separatrices. C2 was north of the X line so magnetospheric elec-

trons propagating along reconnected field lines will have $\theta \gtrsim 90^\circ$ in the magnetosheath separatrix regions. For $E \lesssim 100$ eV, $f_e(E)$ is significantly larger for small θ , corresponding to low-energy electrons drifting toward the X line. This type of electron distribution is responsible for the vertical striations observed in Figure 2b.

We model the electron distributions as a sum of bi-Maxwellian distribution functions

$$f(v_{\parallel}, v_{\perp}) = \sum_j \frac{n_e^j}{(\sqrt{\pi}v_{th}^j)^3} \exp\left(-\left[\frac{v_{\parallel} - v_d^j}{v_{th}^j}\right]^2\right) \cdot \frac{T_{\parallel}^j}{T_{\perp}} \exp\left(-\left[\frac{v_{\perp}^2}{T_{\perp}/T_{\parallel}^j(v_{th}^j)^2}\right]\right), \quad (1)$$

where v_{\parallel} and v_{\perp} are the parallel and perpendicular speeds and n_e^j , v_{th}^j , v_d^j , and $T_{\parallel}^j/T_{\perp}$ are the number density, electron thermal speed, drift velocity parallel (or antiparallel) to \mathbf{B} , and parallel to perpendicular temperature ratio, respectively, for the j th electron plasma component. We model the observed asymmetry in $f_e(E)$ at $\theta = 0^\circ$ and 180° using a nonzero v_d . Typically, we find that three bi-Maxwellians are required to model the unperturbed magnetospheric $f_e(E)$, and additional bi-Maxwellians are required to model the magnetosheath electron beams and partial loss in magnetospheric electrons. Therefore, the resulting distributions differ significantly from a standard bi-Maxwellian distribution function. The fits are performed by hand because the large number of free parameters makes automated methods difficult. The fits are shown in Figure 4 along with the observed data. Using equation (1) we are able to reproduce all the qualitative features of the observed $f_e(E)$, and good quantitative agreement is found for all θ and E .

To investigate the instabilities and mode properties predicted in the separatrix regions we use the dispersion equation solver WHAMP [Rönnmark, 1982]. We use the fits in Figure 4 and the local $|\mathbf{B}|$ as the input parameters. Figures 4c, 4f, and 4i show the whistler dispersion relations and the associated growth rates for each fitted $f_e(E)$. The whistler modes parallel and antiparallel to \mathbf{B} are plotted. In each case the whistler dispersion

relations are similar for both parallel and antiparallel propagating whistlers. However, the growth rate is significantly larger in the antiparallel direction, meaning the whistlers are predicted to propagate antiparallel to \mathbf{B} , as observed in Figure 2. To satisfy the resonance condition the whistlers propagate in the opposite direction to the resonant electrons. In this case the loss cone is around $\theta = 0^\circ$, so the most unstable whistler waves propagate antiparallel to \mathbf{B} . In each case $f_e(E)$ at $\theta = 180^\circ$ is only slightly smaller than $f_e(E)$ at $\theta = 90^\circ$, so growth of whistlers is much smaller parallel to \mathbf{B} . For both whistler wave examples in the magnetospheric separatrix regions, the frequency corresponding to the maximum growth rate is just above $0.5f_{ce}$, consistent with the observed whistlers in Figures 2 and 3.

For the magnetosheath separatrix region example, the dispersion relation has a maximum frequency of $0.44f_{ce}$ and has a maximum growth rate for $f = 0.42f_{ce}$, consistent with the observation of whistlers with $f < 0.5f_{ce}$. The increased density of the magnetosheath electrons causes the frequency of the driven waves to decrease [Li *et al.*, 2011]. Our model calculations show that the wave numbers of the driven whistler waves increases as the density of magnetosheath electrons increases. This maintains gyroresonance with magnetospheric electrons, although v_{ph} decreases.

Solutions to the dispersion equation over a range of perpendicular wave numbers k_\perp show that the growth rate is maximal for $k_\perp = 0$. No growth of quasi-electrostatic oblique whistlers is found. Estimates of the parallel electron plasma beta $\beta_{\parallel e}$ for the resonant electrons are consistent with $\beta_{\parallel e}$ being too large for growth of oblique whistlers to dominate [Gary and Cairns, 1999; Gary *et al.*, 2012].

The properties of the observed whistler waves and the properties predicted by linear theory are shown in Table 2. Very good agreement is found between the observed and predicted whistler waves. This suggests that C2 crossed the separatrix regions close to the whistler source regions because the local $f_e(E)$ accounts for the observed whistler properties. Moreover, the agreement between observations and the calculated dispersion relations indicates that the observed whistlers are generated by the loss-cone distributions at magnetospheric energies and are well explained by linear growth theory.

The electron distributions in the separatrix regions are also unstable to the electrostatic beam mode, due to the beams of electrons propagating parallel to \mathbf{B} . Figures 5a and 5b show the beam mode dispersion relations and growth rates based on the distributions in Figures 4d–4e and Figures 4g–4h, respectively. The beam modes propagate parallel to \mathbf{B} , in the opposite direction to the whistler waves. In the magnetospheric separatrix regions this corresponds to the waves propagating away from the X line, and in the magnetosheath separatrix regions the waves propagate toward the X line. The beam modes are well approximated by the linear dispersion relation $\omega = vk$. Here v is both the phase and group speeds, and k is the wave number. We calculate $v \approx 5 \times 10^3 \text{ km s}^{-1}$ and $v \approx 2.3 \times 10^3 \text{ km s}^{-1}$ for Figures 5a and 5b, respectively. These speeds are well below the phase speeds of the whistler waves. Similarly, the beam modes have much larger k than the whistlers resulting in much shorter wavelengths. Because the wave numbers and speeds of the beam modes differ significantly from the whistlers, the modes likely do not strongly interact with each other. Moreover, since beam modes are generated by beams of magnetosheath electrons and the whistlers are generated by the anisotropic magnetospheric electrons, the growth of beam mode waves should not inhibit whistler growth. The predicted beam mode waves

may account for some of the broadband electric fields extending above f_{ce} in Figure 2d. Beam mode waves are known to evolve into electrostatic solitary waves (ESWs) [Omura *et al.*, 1996], so ESW generation in the magnetospheric and magnetosheath separatrix regions is viable [Cattell *et al.*, 2002; Matsumoto *et al.*, 2003; Graham *et al.*, 2015]. If ESWs develop in the magnetospheric separatrix regions we expect them to propagate away from the X line (in the same direction as the beam), in contrast to symmetric reconnection, where ESWs tend to propagate toward the X line [Cattell *et al.*, 2005; Wang *et al.*, 2014].

4. 22 April 2008

4.1. Overview

The second event we investigate is a magnetopause crossing on 22 April 2008 north of the X line, shown in Figure 6. At this time C2 was located at $(8.8, -5.1, 0.6)R_E$ (GSM). C3 and C4 were approximately $1R_E$ southward of C2 and crossed the ion diffusion region [Graham *et al.*, 2014]. C2 began in the magnetosphere and partially crossed the magnetospheric separatrix regions twice, which are identified by the partial loss in magnetospheric electrons and increase in magnetosheath electrons, as seen in Figure 6b. This indicates regions where the magnetic field lines have reconnected, enabling magnetosheath electrons to enter the magnetosphere. These changes in the electron differential energy fluxes result in the electron temperature decreasing from the magnetospheric value $T_{eMS} = 1400$ eV. Although the electron differential energy fluxes change significantly from the background magnetosphere, \mathbf{B} changes little. The density of the separatrix regions remains comparable to the unperturbed magnetosphere, although in the blue shaded interval n_e increases, indicating that the increase in magnetosheath electrons exceeds the

loss in magnetospheric electrons. However, at these times the density inferred from the spacecraft potential decreases, suggestive of density cavities (Figure 6c). At 18:04:40 UT, C2 crossed the magnetospheric separatrix region into the ion outflow region, then partially crossed the magnetospheric separatrix region at 18:05:05 UT, and re-entered the outflow region. The different regions are identified by the changes in the electron differential energy fluxes and n_e .

At about 18:07:15 UT C2 crossed a current sheet, where we observed a decrease in the electron differential energy fluxes at magnetospheric energies. We interpret this as a crossing from the outflow region to the magnetosheath separatrix region, which bounds the outflow region and the magnetosheath. At 18:07:56 UT, C2 entered the magnetosheath, where negligible electron differential energy fluxes are observed at magnetospheric energies. Therefore, we interpret the region between $\sim 18:07:15$ UT and 18:07:56 UT as the magnetosheath separatrix region. In this region **B** is similar to the magnetosheath **B**. Although vertical striations at the spacecraft spin period are not very pronounced, the electron distributions are anisotropic (section 5). In contrast, the regions identified as the outflow regions tend to have isotropic electron distributions. The times when C2 was located in the magnetosphere, magnetospheric and magnetosheath separatrix regions, ion outflow regions, and the magnetosheath are indicated in Figure 6c.

Figure 6d shows that \mathbf{V}_E is approximately northward between 18:04:40 UT and 18:07:40 UT. This time corresponds to when mixing of magnetospheric and magnetosheath electrons are observed. Throughout this region the density varies but remains comparable to the predicted outflow density $n_{\text{out}} \sim 13 \text{ cm}^{-3}$, based on the magnetospheric and magnetosheath parameters. Both C1 and C3 observed northward ion outflows, Figure 1, reaching

speeds of $\sim 300 \text{ km s}^{-1}$, confirming that C2 crossed the ion outflow region northward of the X line. Based on \mathbf{V} and \mathbf{V}_E obtained from C1 and C3, \mathbf{V}_E significantly underestimates the component of \mathbf{V} in the z-direction. Both C1 and C3 observed similar \mathbf{V}_E to C2 in the outflow regions. From Figure 1 we expect the outflow regions to be primarily observed for $B_z > 0$, i.e., on the magnetospheric side of the current sheet. Therefore, we conclude that the high-density region between $\sim 18:04:45$ UT and $\sim 18:07:15$ UT likely corresponds to the ion outflow region.

In the second partial separatrix crossing, corresponding to the blue shading in Figure 6, narrowband electromagnetic waves are observed, as seen in Figures 6e and 6f. The waves have frequencies between $0.5f_{ce}$ and f_{ce} . Figure 6h shows that the waves are right-hand circularly polarized with respect to the background magnetic field, so we identify them as whistlers. The parallel Poynting vector normalized by its standard deviation (Figure 6i) shows that the whistlers propagate antiparallel to \mathbf{B} . Similar whistler emission is also observed in the separatrix regions observed at $\sim 18:04:40$ UT and $\sim 18:05:05$ UT. Qualitatively, the situation is the same as in the magnetospheric separatrix regions in section 3; whistler emission in the magnetospheric separatrix regions propagates toward the X line. For the observed whistler waves we estimate $v_{ph} = 1.7 \times 10^4 \text{ km s}^{-1}$ from Figure 6f, and $\lambda_{\parallel} = 15 \text{ km}$. For the whistler waves $v_{\parallel res} = 7.7 \times 10^4 \text{ km s}^{-1}$, or equivalently $E = 170 \text{ eV}$, significantly smaller than $T_{eMS} = 1400 \text{ eV}$ but larger than $T_{eSH} = 40 \text{ eV}$. Because \mathbf{E} is not measured along the spacecraft spin axis the estimated v_{ph} , λ_{\parallel} , and $v_{\parallel res}$ may represent lower bounds. In the first partial separatrix region crossing negligible whistler waves are observed. We also observe whistler waves in the outflow region and magnetosheath separatrix region with $f < 0.5f_{ce}$ and lower v_{ph} , similar to those observed in section 3.

Throughout the entire interval in Figure 6, the wave-normal angle θ_k of the whistler waves (not shown) remains close to zero, corresponding to propagation approximately parallel (or antiparallel) to \mathbf{B} . No whistler emission is observed in the magnetosphere near the magnetospheric separatrix regions. In both partial separatrix region crossings broadband electrostatic waves are observed in Figure 6e, which are most intense at low frequencies and extend above f_{ce} . Broadband fluctuations are also observed in the outflow region, and magnetosheath separatrix region, but have lower intensities in the magnetosheath.

4.2. Electron Distributions and Instabilities

In this subsection we investigate in detail the electron distributions observed in the second separatrix region crossing and the associated instabilities. Figure 7 shows $f_e(E)$ between 18:03:38 UT and 18:03:54 UT, corresponding to the blue shaded region in Figure 6. The distributions are recorded over successive spacecraft spins, showing the evolution of $f_e(E)$ with position. Overplotted are our fits to the data using equation (1). We are able to reproduce all the qualitative features and good quantitative agreement is found for all θ and E . Figures 7a and 7b show $f_e(E)$ just before C2 crossed into the separatrix region, and is comparable to the unperturbed magnetospheric $f_e(E)$. For thermal energies $E \gtrsim 200$ eV there is a small temperature anisotropy, $T_\perp > T_\parallel$. For $\theta = 0^\circ$ and 180° , $f_e(E)$ is approximately equal for all E , meaning there is no partial loss in magnetospheric electrons.

The electron distributions in the separatrix region are shown in Figures 7c–7h. The separatrix region is characterized by a field-aligned beam of magnetosheath electrons propagating away from the X line and a decrease in the magnetospheric electrons, primarily for $\theta < 90^\circ$. The loss in magnetospheric electrons with $E \gtrsim 1$ keV at pitch angles close to 0°

producing a loss-cone distribution, which is greatest in Figures 7e–7f. The electron beam decreases in speed and tends to increase in density with time. Based on the fits we obtain $v_b = 250 \text{ eV}$, 130 eV , and 40 eV , and beam number densities $n_b = 0.06 \text{ cm}^{-3}$, 0.05 cm^{-3} , and 0.15 cm^{-3} for Figures 7c–7d, 7e–7f, and 7g–7h, respectively. The distributions have the same qualitative features as those in Figures 4d and 4e.

Two modes are found with a positive growth rate in the separatrix region; the electromagnetic whistler mode and the electrostatic beam mode. Both modes are aligned with **B** and have maximum growth rates for $k_\perp = 0$. In each case $\beta_{\parallel e}$ is too large for oblique whistlers to form. Figure 8 shows the dispersion relation, growth rate, and v_{ph} of two the modes. For all four electron distributions the whistler mode is found; however, it only has a positive growth rate for the second and third electron distributions, when the loss in parallel propagating magnetospheric electrons is greatest. The whistler waves are not driven by the distribution in Figures 7a–7b, meaning the local temperature anisotropy in the magnetosphere ($T_\perp/T_\parallel \approx 1.3$) is too small to drive whistler waves, which is consistent with observations. In Figures 7c–7f the growth rate is positive for whistlers parallel and antiparallel to **B**. However, the growth rate is significantly larger antiparallel to **B** because the loss cone is in the parallel direction. This is consistent with the observed whistlers propagating toward the X line. For the whistler waves associated with Figures 7e–7f, when the growth is maximal, the frequencies of the growing whistler waves are $0.4 \lesssim \omega/\Omega_{ce} \lesssim 0.7$, or equivalently $700 \text{ Hz} \lesssim f \lesssim 1200 \text{ Hz}$, which partially overlaps with the frequency range of the whistlers observed in Figure 6. In Figures 6e and 6f the whistlers in this region have maximum powers at $f \sim 1100 \text{ Hz}$.

The beam mode waves may explain the observed broadband electric fields observed in the separatrix regions. Beam mode waves can potentially form ESWs, which are frequently observed at the magnetopause and in the separatrix regions of magnetic reconnection [Cattell *et al.*, 2002; Matsumoto *et al.*, 2003; Graham *et al.*, 2015]. The maximum growth rate is found for the distribution in Figures 7c–7d, when the beam speed is largest. For the distributions in Figures 7e–7f and Figures 7g–7h, the beam speed is slower and the beam mode growth rate significantly decreases. The wave numbers of the unstable whistler waves are an order of magnitude smaller than the unstable beam mode wave numbers, and the waves propagate in opposite directions. Moreover, the dispersion relations only cross at $k_{\parallel} \approx 0$, meaning the two modes are distinct from each other. Based on the predicted beam mode properties, the whistler waves observed here cannot be produced by Čerenkov emission [Goldman *et al.*, 2014]. Similarly, the whistlers have larger v_{ph} than any of the beam modes, as shown in Figures 8e and 8f. In model calculations where the electron beam is removed the whistlers still exhibit positive growth, so the observed whistlers are not generated by the electron beam. This differs from symmetric reconnection, where electron beams propagating toward the diffusion region can generate whistlers [Fujimoto, 2014]. Figure 8d shows that the beam mode growth rate is much larger than the whistler growth, leading to rapid saturation of the beam instability. Since the beam is not responsible for whistler growth, beam saturation by the beam mode waves should not impede whistler growth. This may explain why electrostatic fluctuations and whistler waves are observed simultaneously in the magnetospheric separatrix regions.

Although the electron beams do not excite the observed whistler waves, they can affect the whistler growth rate. In particular, model calculations of the whistler growth

rate in the presence of cold isotropic electrons show that the growth rate increases as the density of cold electron increases [Gary *et al.*, 2012; Wu *et al.*, 2013]. Here, the presence of cold isotropic electrons (used to model the lowest energy electrons) and the electron beam causes the growth rate to increase. Calculations of the dispersion relations without the cold electrons and electron beam yield smaller growth rates for the whistler waves. Therefore, the presence of magnetosheath electrons favors whistler growth in the magnetospheric separatrix regions.

In conclusion, the magnetospheric separatrix regions are resolved over multiple space-craft spins, allowing the spatial evolution of $f_e(E)$ to be investigated. Within the magnetospheric separatrix regions electromagnetic whistler waves are observed. The electron distributions are unstable to the electromagnetic whistler wave and the electrostatic beam mode. Table 2 compares the observed and predicted whistler properties. The predicted frequencies partially overlap with the observed frequencies. However, the predicted v_{ph} and parallel wavelength λ_{\parallel} are larger than the observed values. In this case the observed v_{ph} could be underestimated because \mathbf{E} is not measured along the spacecraft spin axis. The whistler waves could be excited in the separatrix region northward of the spacecraft then propagate past C2 toward the X line. Nevertheless, we conclude that the observed whistler waves are excited by the loss of magnetospheric electrons propagating away from the X line, which produces a loss-cone distribution at magnetospheric energies.

5. Discussion

The results presented in sections 3 and 4 confirm many of the results in Stenberg *et al.* [2005] and Stenberg *et al.* [2007]. Namely, that whistlers are generated by electron anisotropies caused by a partial loss of magnetospheric electrons. Using detailed fits

to the observed distributions we are able to reproduce the properties and propagation direction of the observed whistlers. We identified these regions as the separatrix regions of asymmetric reconnection near the subsolar point. We also found that beams of magnetosheath electrons develop in the magnetospheric separatrix regions, which propagate away from the diffusion region.

We now investigate the causes of the anisotropic distributions in the reconnection separatrix regions. Figure 9 (top panel) shows a diagram of magnetic reconnection at the magnetopause, adapted from Figure 3 of *Graham et al.* [2014]. Overplotted are the expected electric fields \mathbf{E}_{\parallel} parallel to \mathbf{B} for asymmetric reconnection [*Egedal et al.*, 2011], and the expected electron trajectories to produce the observed $f_e(E)$. Figure 9 also shows electron distributions observed in the separatrix regions, ion diffusion region, and ion outflow region for the 22 April 2008 reconnection event and compares them with the unperturbed magnetospheric and magnetosheath electron distributions.

Figure 9a shows $f_e(E)$ from the partial separatrix region crossing in Figure 7e and compares it with the unperturbed angle-averaged magnetospheric and magnetosheath $f_e(E)$. For $E \gtrsim 500$ eV a loss-cone distribution develops near $\theta = 0^\circ$, corresponding a loss in magnetospheric electrons propagating away from the X line. The beam of field-aligned magnetosheath electrons is present at $E \sim 100$ eV, corresponding to magnetosheath electrons propagating away from the X line. The electron beams have speeds below the magnetospheric thermal speed so they are unable to fill the loss cone in the magnetospheric electron distribution, making the distribution unstable to whistler emission. However, the fact that $f_e(E)$ exceeds the magnetosheath $f_e(E)$ near $E = 200$ eV indicates that some of the magnetosheath electrons have been accelerated. The expected trajectories

of electrons resulting in the observed distribution are shown in Figure 9. We expect the beam of magnetosheath electrons to form from electrons propagating parallel to \mathbf{B} from the magnetosheath (dark blue lines in Figure 9). The parallel electric fields on both sides of the diffusion region will tend to reflect electrons, significantly reducing the density of sheath electrons, as they propagate toward the magnetospheric separatrix regions along \mathbf{B} . However, to produce the observed electron beams these passing electrons must be accelerated. Such acceleration could be caused by the reconnection electric field or could occur outside the ion diffusion region on the magnetospheric side if \mathbf{E}_{\parallel} points toward the X line.

The generation of whistlers in the separatrix regions of asymmetric reconnection differs from symmetric reconnection. In general, electron beam distributions and counterstreaming electron distributions are reported in the separatrix regions of magnetic reconnection in the magnetotail [Deng *et al.*, 2004; Viberg *et al.*, 2013]. Similarly, observations and simulations of symmetric reconnection found that whistlers were generated by electron beams [Zhang *et al.*, 1999; Wei *et al.*, 2007; Teste and Parks, 2009; Fujimoto, 2014]. In contrast, we find that for asymmetric reconnection at Earth's magnetopause the whistler waves are generated by loss-cone distributions, which develop because the reconnecting plasmas have distinct temperatures; magnetosheath electrons are unable to fill the loss cone in the magnetospheric separatrix regions. We conclude that the generation mechanisms of whistler waves can differ between symmetric and asymmetric reconnection.

The electron distributions in the ion outflow region (e.g., Figure 9b) typically consist of approximately isotropic magnetospheric and magnetosheath electrons, consistent with pitch-angle scattering of the inflowing electrons passing close to the X line, where \mathbf{B} is

reduced [Le *et al.*, 2010]. The magnetosheath electrons have been slightly heated compared with the unperturbed magnetosheath $f_e(E)$. We note that outflow regions are often highly turbulent and anisotropic distributions can develop, which can then excite whistler waves, for instance, where magnetic flux piles up [Fujimoto and Sydora, 2008] or near magnetic islands [Shuster *et al.*, 2014]. This may account for some of the whistler emission observed in the outflow regions in Figures 2 and 6.

Figure 9c shows $f_e(E)$ in the magnetosheath separatrix region, compared with the unperturbed magnetospheric and magnetosheath $f_e(E)$. At $\theta = 0^\circ$, corresponding to electrons propagating toward the X line, $f_e(E)$ is comparable to the magnetosheath $f_e(E)$. For $E \gtrsim 1$ keV, $f_e(E)$ is below the instrumental one count level, meaning no magnetospheric electrons are observed propagating toward the X line. For $\theta \gtrsim 90^\circ$, $f_e(E)$ exceeds the magnetosheath $f_e(E)$ for $E \gtrsim 50$ eV, and exceeds the instrumental one-count level for $E > 1$ keV, indicating magnetospheric electrons propagating away from the X line. Northward of the X line we expect magnetospheric electrons with $\theta \gtrsim 90^\circ$ to propagate along the reconnected field lines into the magnetosheath. The anisotropy at lower energies $E \sim 100$ eV may indicate that some magnetosheath electrons have been accelerated away from the X line. For $E \lesssim 50$ eV, $f_e(E)$ is largest for $\theta = 0^\circ$, indicating a drift of low-temperature electrons toward the X line. This anisotropy is more evident in Figures 4g and 4h.

Figure 9d shows $f_e(E)$ observed by C3 and C4 in the ion diffusion region [Graham *et al.*, 2014]. The ion diffusion region is characterized by mixing of magnetospheric and magnetosheath electrons, although the densities are significantly smaller than their respective unperturbed densities. The magnetosheath electrons are heated parallel to \mathbf{B} , resulting

in an increased parallel pressure, which is characteristic of the ion diffusion region [Le *et al.*, 2010]. The flat-top distribution for $\theta = 0^\circ$ and 180° at low E is consistent with a parallel potential $\Phi_{\parallel} \approx 150$ V trapping magnetosheath electron in the ion diffusion region [Graham *et al.*, 2014]. The expected trajectory of a trapped magnetosheath electron is shown in Figure 9 with the pink line. The magnetospheric electrons are too energetic to be significantly affected by Φ_{\parallel} . Therefore, the temperature anisotropy at magnetospheric energies is relatively small.

We now discuss the effects of the generated whistler emission on asymmetric reconnection. Once generated the whistler waves will tend to isotropize the magnetospheric electrons as the waves are damped. However, while asymmetric reconnection is ongoing whistlers can potentially be continuously driven by escape of magnetospheric electrons. Therefore, the observed electron anisotropy in the magnetospheric separatrix regions depends on two competing processes, viz., ongoing asymmetric reconnection, which generates the loss-cone distribution, and scattering of electrons by whistler waves, which tends to isotropize the resonant electrons and fill the loss cone. Because the electron distributions generating the observed whistlers are produced by ongoing magnetic reconnection, the growth of whistlers propagating toward the X line is only expected after reconnection has been initiated. Based on the properties of the whistlers in the separatrix regions, whistlers should only significantly scatter electrons with magnetospheric energies, whereas the magnetosheath electrons develop the parallel electron heating in the ion diffusion region (Figure 9d) [Graham *et al.*, 2014]. For the 2008 April 22 event no whistlers were observed by C3 and C4 in the diffusion region, so whistlers likely do not influence magnetic reconnection in the electron or ion diffusion regions for this event. However, whistler

waves have been reported near the electron diffusion region of asymmetric reconnection [Tang *et al.*, 2013]. Tang *et al.* [2013] found that the whistlers generated near the electron diffusion region propagate away from the X line, in contrast to the whistlers generated in the magnetospheric separatrix regions reported here. This difference in the propagation direction may be because the whistler waves are generated in different regions.

Electron scattering by the whistler waves could nevertheless affect the large-scale parallel electric fields, near the diffusion region. These fields extend outside the electron diffusion region and are responsible for electron trapping in the ion diffusion region [Egedal *et al.*, 2008, 2011]. Therefore, whistler waves could modify the parallel electric field and hence trapping of magnetosheath electrons. Such effects could modify the electron pressure anisotropy in the diffusion region. Future work is required to investigate how whistler waves generated in the separatrix regions affect ongoing reconnection.

6. Conclusions

In this paper we have investigated the generation of whistler waves in the separatrix regions of asymmetric magnetic reconnection at the dayside magnetopause. We observe whistlers in the magnetospheric and magnetosheath separatrix regions and the outflow regions. The key results are:

- (1) The most intense whistler emission associated with asymmetric reconnection is observed in the magnetospheric separatrix regions. Whistler emission is also observed in the magnetosheath separatrix regions and outflow regions.
- (2) The magnetospheric separatrix regions are typically characterized by a beam of magnetosheath electrons propagating away from the X line and a loss in magnetospheric electrons propagating away from the X line. The magnetosheath separatrix regions are

characterized by a cold magnetosheath population drifting toward the X line and higher energy electrons propagating away from the X line, consisting of accelerated magnetosheath electrons and magnetospheric electrons propagating along reconnected magnetic field lines.

(3) In the magnetospheric separatrix regions the observed whistlers propagate toward the X line. The whistler waves are generated by the loss in magnetospheric electrons propagating away from the X line, which produces loss-cone distributions at magnetospheric energies. These distributions are unstable to whistler waves, which propagate toward the X line. Although electron beams are often observed simultaneously with whistlers, the beams do not drive the observed whistler emission.

(4) The linear whistler waves predicted for the observed electron distributions agree well with observations, showing that the observed whistlers are generated by loss-cone distributions, and are well explained by linear growth theory. The increased density of cold magnetosheath electrons tends to increase the whistler growth rate, making the magnetospheric separatrix regions favorable for whistler emission.

(5) Beam-mode waves are predicted in the magnetospheric and magnetosheath separatrix regions, which may account for the observed broadband electric fields and potentially lead to the formation of ESWs. The resonant electron energies of the beam mode and whistler mode do not overlap, so beam mode generation and the associated electrostatic fields do not inhibit whistler growth.

The results presented in this paper show that the temperature difference between the reconnecting plasmas can affect the type of instabilities that develop in the separatrix regions. In particular, the temperature difference is important for whistler generation.

The results of this paper can be further investigated with the Magnetospheric Multiscale (MMS) mission, where higher time resolution electron data will be available and the spacecraft will be more closely separated, enabling more detailed investigations of the structure of the separatrix regions associated with asymmetric reconnection.

Acknowledgments. We thank the ESA Cluster Science Archive team and the Cluster PI teams for data access and support. The data used in this study were provided by the Cluster Science Archive (<http://www.cosmos.esa.int/web/csa>). This work receives EU support through the FP7-Space grant agreement 284520 for the MAARBLE collaborative research project. This work was supported by the Swedish National Space Board, Grant Nos. 128/11:2 and 77/13.

References

- André, M., A. Vaivads, S. C. Buchert, A. N. Fazakerley, and A. Lahiff (2004), Thin electron-scale layers at the magnetopause, *Geophys. Res. Lett.*, *31*, L03,803, doi: 10.1029/2003GL018137.
- André, M., A. Vaivads, Y. V. Khotyaintsev, T. Laitinen, H. Nilsson, G. Stenberg, A. Fazakerley, and J. G. Trotignon (2010), Magnetic reconnection and cold plasma at the magnetopause, *Geophys. Res. Lett.*, *37*, L22,108, doi:10.1029/2010GL044611.
- Baumjohann, W., R. A. Treumann, E. Georgescu, G. Haerendel, K.-H. Fornacon, and U. Auster (1999), Waveform and packet structure of lion roars, *Ann. Geophys.*, *17*, 1528, doi:10.1007/s00585-999-1528-9.
- Bell, T. F., and O. Buneman (1964), Plasma instability in the whistler mode caused by a gyrating electron stream, *Phys. Rev.*, *133*, 1300, doi:10.1103/PhysRev.133.A1300.

- Birn, J., et al. (2001), Geospace environmental modeling (GEM) magnetic reconnection challenge, *J. Geophys. Res.*, *106*, 3715, doi:10.1029/1999JA900449.
- Cassak, P. A., and M. A. Shay (2007), Scaling of asymmetric magnetic reconnection: General theory and collisional simulations, *Phys. Plasmas*, *14*, 102,114, doi:10.1063/1.2795630.
- Cattell, C., J. Crumley, J. Dombeck, J. Wygant, and F. S. Mozer (2002), Polar observations of solitary waves at the earth's magnetopause, *Geophys. Res. Lett.*, *29*, 1065, doi:10.1029/2001GL014046.
- Cattell, C., et al. (2005), Cluster observations of electron holes in association with magnetotail reconnection and comparison to simulations, *J. Geophys. Res.*, *110*, A01,211, doi:10.1029/2004JA010519.
- Chaston, C. C., et al. (2005), Drift-kinetic Alfvén waves observed near a reconnection X line in the Earth's magnetopause, *Phys. Rev. Lett.*, *95*, 065,002, doi:10.1103/PhysRevLett.95.065002.
- Deng, X. H., and H. Matsumoto (2001), Rapid magnetic reconnection in the Earth's magnetosphere mediated by whistler waves, *Nature*, *410*, 557, doi:10.1038/35069018.
- Deng, X. H., H. Matsumoto, H. Kojima, T. Mukai, R. R. Anderson, W. Baumjohann, and R. Nakamura (2004), Geotail encounter with reconnection diffusion region in the Earth's magnetotail: Evidence of multiple X lines collisionless reconnection?, *J. Geophys. Res.*, *109*, A05,206, doi:10.1029/2003JA010031.
- Divin, A., G. Lapenta, S. Markidis, D. L. Newman, and M. V. Goldman (2012), Numerical simulations of separatrix instabilities in collisionless magnetic reconnection, *Phys. Plasmas*, *19*, 042,110, doi:10.1063/1.3698621.

- Egedal, J., W. Fox, N. Katz, M. Porkolab, M. Oieroset, R. P. Lin, W. Daughton, and J. F. Drake (2008), Evidence and theory for trapped electrons in guide field magnetotail reconnection, *J. Geophys. Res.*, 113, A12,207, doi:10.1029/2008JA013520.
- Egedal, J., A. Le, P. L. Pritchett, and W. Daughton (2011), Electron dynamics in two-dimensional asymmetric anti-parallel reconnection, *Phys. Plasmas*, 18, 102,901, doi: 10.1063/1.3646316.
- Escoubet, C. P., M. Fehringer, and M. Goldstein (2001), Introduction: The Cluster mission, *Ann. Geophys.*, 19, 1197, doi:10.5194/angeo-19-1197-2001.
- Farrell, W. M., M. D. Desch, M. L. Kaiser, and K. Goetz (2002), The dominance of electron plasma waves near a reconnection X-line region, *Geophys. Res. Lett.*, 29, 1902, doi:10.1029/2002GL014662.
- Fujimoto, K. (2014), Wave activities in separatrix regions of magnetic reconnection, *Geophys. Res. Lett.*, 41, 2721, doi:10.1002/2014GL059893.
- Fujimoto, K., and R. D. Sydora (2008), Whistler waves associated with magnetic reconnection, *Geophys. Res. Lett.*, 35, L19,112, doi:10.1029/2008GL035201.
- Fujimoto, M., I. Shinohara, and H. Kojima (2011), Reconnection and waves: A review with a perspective, *Space Sci. Rev.*, 160, 123, doi:10.1007/s11214-011-9807-7.
- Gary, S. P., and I. H. Cairns (1999), Electron temperature anisotropy instabilities: Whistler, electrostatic and z mode, *J. Geophys. Res.*, 104, 19,835, doi: 10.1029/1999JA900296.
- Gary, S. P., E. E. Scime, J. L. Phillips, and W. C. Feldman (1994), The whistler heat flux instability: Threshold conditions in the solar wind, *J. Geophys. Res.*, 99, 23,391, doi:10.1029/94JA02067.

Gary, S. P., K. Liu, R. E. Denton, and S. Wu (2012), Whistler anisotropy instability with a cold electron component: Linear theory, *J. Geophys. Res.*, 117, A07,203, doi: 10.1029/2012JA017631.

Goldman, M. V., D. L. Newman, and P. Pritchett (2008), Vlasov simulations of electron holes driven by particle distributions for PIC reconnection simulations with a guide field, *Geophys. Res. Lett.*, 35, L22,109, doi:10.1029/2008GL035608.

Goldman, M. V., D. L. Newman, G. Lapenta, L. Andersson, J. T. Gosling, S. Eriksson, S. Markidis, J. P. Eastwood, and R. Ergun (2014), Čerenkov emission of quasiparallel whistlers by fast electron phase-space holes during magnetic reconnection, *Phys. Rev. Lett.*, 112, 145,002, doi:10.1103/PhysRevLett.112.145002.

Gosling, J. T., J. R. Asbridge, S. J. Bame, W. C. Feldman, G. Paschmann, N. Sckopke, and C. T. Russell (1982), Evidence for quasi-stationary reconnection at the dayside magnetopause, *J. Geophys. Res.*, 87, 2147, doi:10.1029/JA087iA04p02147.

Gosling, J. T., M. F. Thomsen, S. J. Bame, T. G. Onsager, and C. T. Russell (1990), The electron edge of the low latitude boundary layer during accelerated flow events, *Geophys. Res. Lett.*, 17, 1833, doi:10.1029/GL017i011p01833.

Graham, D. B., Y. V. Khotyaintsev, A. Vaivads, M. André, and A. N. Fazakerley (2014), Electron dynamics in the diffusion region of an asymmetric magnetic reconnection, *Phys. Rev. Lett.*, 112, 215,004, doi:10.1103/PhysRevLett.112.215004.

Graham, D. B., Y. V. Khotyaintsev, A. Vaivads, and M. André (2015), Electrostatic solitary waves with distinct speeds associated with asymmetric reconnection, *Geophys. Res. Lett.*, 42, 215, doi:10.1002/2014GL062538.

- Gurnett, D. A., L. A. Frank, and R. P. Lepping (1976), Plasma waves in the distant magnetotail, *J. Geophys. Res.*, *81*, 6059, doi:10.1029/JA081i034p06059.
- Kennel, C. F., and H. E. Petschek (1966), Limit on stably trapped particle fluxes, *J. Geophys. Res.*, *71*, 1–28, doi:10.1029/JZ071i001p00001.
- Khotyaintsev, Y. V., A. Vaivads, A. Retinò, M. André, C. J. Owen, and H. Nilsson (2006), Formation of inner structure of a reconnection separatrix region, *Phys. Rev. Lett.*, *97*, 205,003, doi:10.1103/PhysRevLett.97.205003.
- Le, A., J. Egedal, W. Fox, N. Katz, A. Vrblevskis, W. Daughton, and J. F. Drake (2010), Equations of state in collisionless magnetic reconnection, *Phys. Plasmas*, *17*, 055,703, doi:10.1063/1.3309425.
- Li, W., J. Bortnik, R. M. Thorne, Y. Nishimura, V. Angelopoulos, and L. Chen (2011), Modulation of whistler mode chorus waves: 2. Role of density variations, *J. Geophys. Res.*, *116*, A06,206, doi:10.1029/2010JA016313.
- Lindstedt, T., Y. V. Khotyaintsev, A. Vaivads, M. André, R. C. Fear, B. Lavraud, S. Haaland, and C. J. Owen (2009), Separatrix regions of magnetic reconnection at the magnetopause, *Ann. Geophys.*, *27*, 4039, doi:10.5194/angeo-27-4039-2009.
- Matsumoto, H., X. H. Deng, H. Kojima, and R. R. Anderson (2003), Observation of electrostatic solitary waves associated with reconnection on the dayside magnetopause boundary, *Geophys. Res. Lett.*, *30*, 59–1, doi:10.1029/2002GL016319.
- Mozer, F. S., S. D. Bale, and T. D. Phan (2002), Evidence of diffusion regions at a subsolar magnetopause crossing, *Phys. Rev. Lett.*, *89*, 015,002.
- Mozer, F. S., V. Angelopoulos, J. Bonnell, K. H. Glassmeier, and J. P. McFadden (2008), THEMIS observations of modified Hall fields in asymmetric magnetic field reconnection,

Geophys. Res. Lett., 35, L17S04.

Øieroset, M., T. D. Phan, M. Fujimoto, R. P. Lin, and R. P. Lepping (2001), In situ detection of collision less reconnection in the Earth's magnetotail, *Nature*, 412, 414, doi:10.1038/35086520.

Omura, Y., H. Matsumoto, T. Miyake, and H. Kojima (1996), Electron beam instabilities as generation mechanism of electrostatic solitary waves in the magnetotail, *J. Geophys. Res.*, 101, 2685, doi:10.1029/95JA03145.

Paschmann, G., G. Harendel, I. Papamastorakis, N. Sckopke, S. J. Bame, J. T. Gosling, and C. T. Russell (1982), Plasma and magnetic field characteristics of magnetic flux transfer events, *J. Geophys. Res.*, 87, 2159, doi:10.1029/JA087iA04p02159.

Petkaki, P., M. P. Freeman, and A. P. Walsh (2006), Cluster observations of broadband electromagnetic waves in and around a reconnection region in the Earth's magnetotail current sheet, *Geophys. Res. Lett.*, 33, L16,105, doi:10.1029/2006GL027066.

Priest, E. R., and T. Forbes (2000), *Magnetic Reconnection: MHD Theory and Applications*, Cambridge University Press.

Pritchett, P. L. (2008), Collisionless magnetic reconnection in an asymmetric current sheet, *J. Geophys. Res.*, 113, A06,210, doi:10.1029/2007JA012930.

Retinò, A., et al. (2006), Structure of the separatrix region close to a magnetic reconnection X-line: Cluster observations, *Geophys. Res. Lett.*, 33, L06,101, doi: 10.1029/2005GL024650.

Rönnmark, K. (1982), WHAMP – Waves in homogeneous, anisotropic, multicomponent plasmas, *technical report, Kiruna Geophys. Inst., Kiruna, Sweden*.

- Santolík, O., D. A. Gurnett, J. S. Pickett, M. Parrot, and N. Cornilleau-Wehrlin (2004), A microscopic and nanoscopic view of storm-time chorus on 31 March 2001, *Geophys. Res. Lett.*, 31, L02,801, doi:10.1029/2003GL018757.
- Santolík, O., C. A. Kletzing, W. S. Kurth, G. B. Hospodarsky, and S. R. Bounds (2014), Fine structure of large-amplitude chorus wave packets, *Geophys. Res. Lett.*, 41, 293, doi:10.1002/2013GL058889.
- Shuster, J. R., L.-J. Chen, W. S. Daughton, L. C. Lee, K. H. Lee, N. Bessho, R. B. Torbert, G. Li, and M. R. Argall (2014), Highly structured electron anisotropy in collisionless reconnection exhausts, *Geophys. Res. Lett.*, 41, doi:10.1002/2014GL060608.
- Sonnerup, B. U. O., G. Paschmann, I. Papamastorakis, N. Sckopke, G. Haerendel, S. J. Bame, J. R. Asbridge, J. T. Gosling, and C. T. Russell (1981), Evidence for magnetic field reconnection at the Earth's magnetopause, *J. Geophys. Res.*, 86, 10,049.
- Stenberg, G., T. Oscarsson, M. André, A. Vaivads, M. Morooka, N. Cornilleau-Wehrlin, A. Fazakerley, B. Lavraud, and P. M. E. Décréau (2005), Electron-scale sheets of whistlers close to the magnetopause, *Ann. Geophys.*, 23, 3715, doi:10.5194/angeo-23-3715-2005.
- Stenberg, G., et al. (2007), Internal structure and spatial dimensions of whistler wave regions in the magnetopause boundary layer, *Ann. Geophys.*, 25, 2439, doi:10.5194/angeo-25-2439-2007.
- Swisdak, M., B. N. Rogers, J. F. Drake, and M. A. Shay (2003), Diamagnetic suppression of component magnetic reconnection at the magnetopause, *J. Geophys. Res.*, 108, 1218, doi:10.1029/2002JA009726.

Tanaka, K. G., et al. (2008), Effects on magnetic reconnection of a density asymmetry across the current sheet, *Ann. Geophys.*, *26*, 2471, doi:10.5194/angeo-26-2471-2008.

Tang, X., C. Cattell, J. Dombeck, L. Dai, L. B. Wilson III, A. Breneman, and A. Hupach (2013), THEMIS observations of the magnetopause electron diffusion region: Large amplitude waves and heated electrons, *Geophys. Res. Lett.*, *40*, 2884, doi:10.1002/grl.50565.

Teste, A., and G. K. Parks (2009), Counterstreaming beams and flat-top electron distributions observed with Langmuir, whistler, and compressional Alfvén waves in Earth's magnetic tail, *Phys. Rev. Lett.*, *102*, 075,003, doi:10.1103/PhysRevLett.102.075003.

Vaivads, A., O. Santolík, G. Stenberg, M. André, C. J. Owen, P. Canu, and M. Dunlop (2007), Source of whistler emissions at the dayside magnetopause, *Geophys. Res. Lett.*, *34*, L09,106, doi:10.1029/2006GL029195.

Viberg, H., Y. V. Khotyaintsev, A. Vaivads, M. André, and J. S. Pickett (2013), Mapping HF waves in the reconnection diffusion region, *Geophys. Res. Lett.*, *40*, 1032, doi:10.1002/grl.50227.

Viberg, H., Y. V. Khotyaintsev, A. Vaivads, M. André, H. S. Fu, and N. Cornilleau-Wehrlin (2014), Whistler mode waves at magnetotail dipolarization fronts, *J. Geophys. Res.*, *119*, 2605, doi:10.1002/2014JA019892.

Wang, R., et al. (2012), Asymmetry in the current sheet and secondary magnetic flux ropes during guide field magnetic reconnection, *J. Geophys. Res.*, *117*, A07,223, doi: 10.1029/2011JA017384.

Wang, R., et al. (2013), Observation of multiple sub-cavities adjacent to single separatrix, *Geophys. Res. Lett.*, *40*, 2511, doi:10.1002/grl.50537.

Wang, R., et al. (2014), Observation of double layer in the separatrix region during magnetic reconnection, *Geophys. Res. Lett.*, *41*, 4851, doi:10.1002/2014GL061157.

Wei, X. H., et al. (2007), Cluster observations of waves in the whistler frequency range associated with magnetic reconnection in the Earth's magnetotail, *J. Geophys. Res.*, *112*, A10,225, doi:10.1029/2006JA011771.

Wu, S., R. E. Denton, and W. Li (2013), Effects of cold electron density on the whistler anisotropy instability, *J. Geophys. Res.*, *118*, 765, doi:10.1029/2012JA018402.

Zhang, Y., H. Matsumoto, and H. Kojima (1999), Whistler mode waves in the magnetotail, *J. Geophys. Res.*, *104*, 28,633, doi:10.1029/1999JA900301.

Zhou, M., et al. (2009), Observation of waves near lower hybrid frequency in the reconnection region with thin current sheet, *J. Geophys. Res.*, *114*, A02,216, doi: 10.1029/2008JA013427.

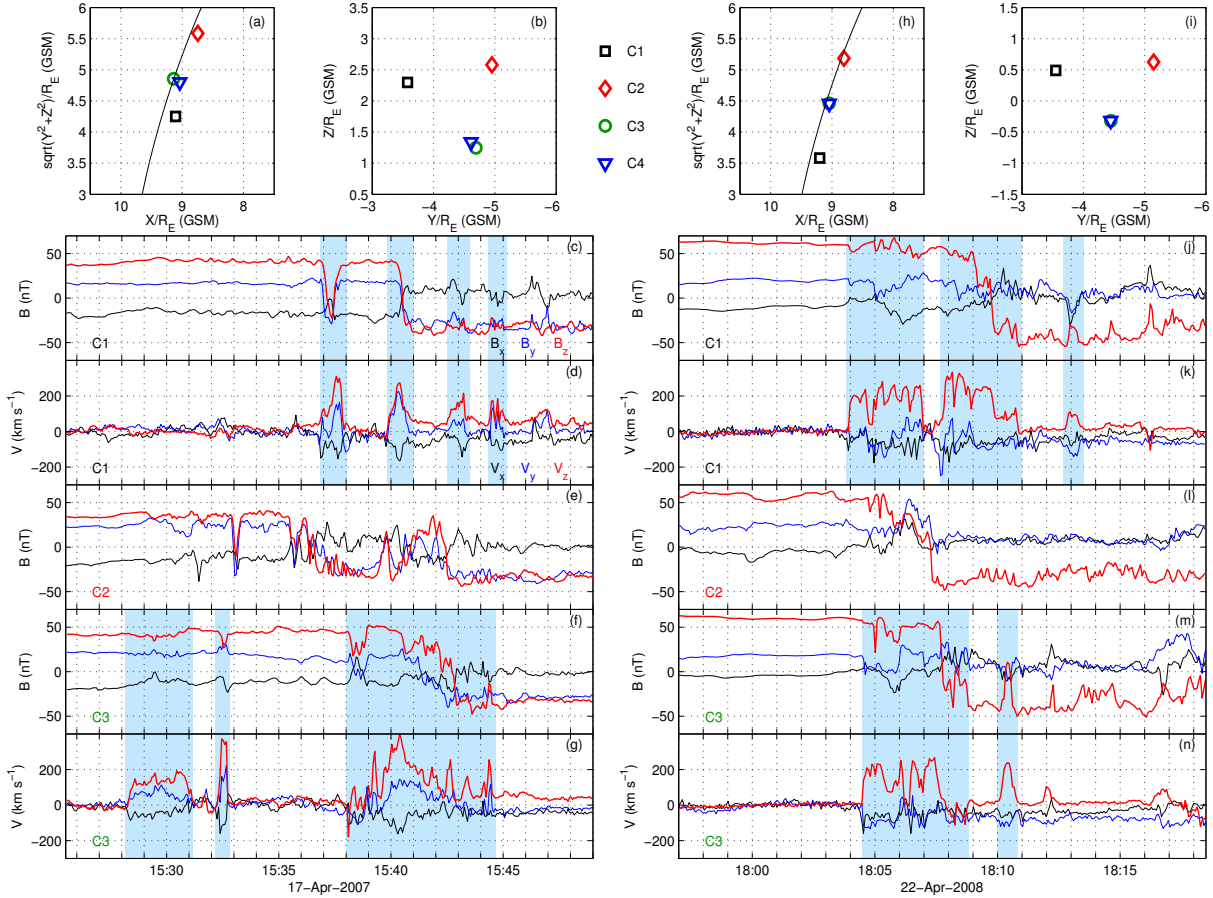


Figure 1. Spacecraft positions, magnetic fields \mathbf{B} , and ion velocities \mathbf{V} for the magnetopause crossings on 17 April 2007 (panels (a)–(g), left side) and 22 April 2008 (panels (h)–(n), right side). (a) and (h) shows the spacecraft positions $\sqrt{Y^2 + Z^2}$ versus X (GSM) and the assumed magnetopause (black line). (b) and (i) show the spacecraft positions Z versus Y (GSM). From top to bottom the remaining panels are: \mathbf{B} from C1, \mathbf{V} from C1, \mathbf{B} from C2, \mathbf{B} from C3, and \mathbf{V} from C3. All data are presented in GSM coordinates. The blue shaded regions indicated the ion outflow regions observed by C1 and C3.

Table 1. Ratios $B_{\text{MS}}/B_{\text{SH}}$, $n_{\text{MS}}/n_{\text{SH}}$, and $T_{e\text{MS}}/T_{e\text{SH}}$, and shear angle θ_s for the two reconnection events based on C2 data.

Event	$B_{\text{MS}}/B_{\text{SH}}$	$n_{\text{MS}}/n_{\text{SH}}$	$T_{e\text{MS}}/T_{e\text{SH}}$	θ_s
17 April 2007	0.97	0.040	49	160°
22 April 2008	1.3	0.023	39	140°

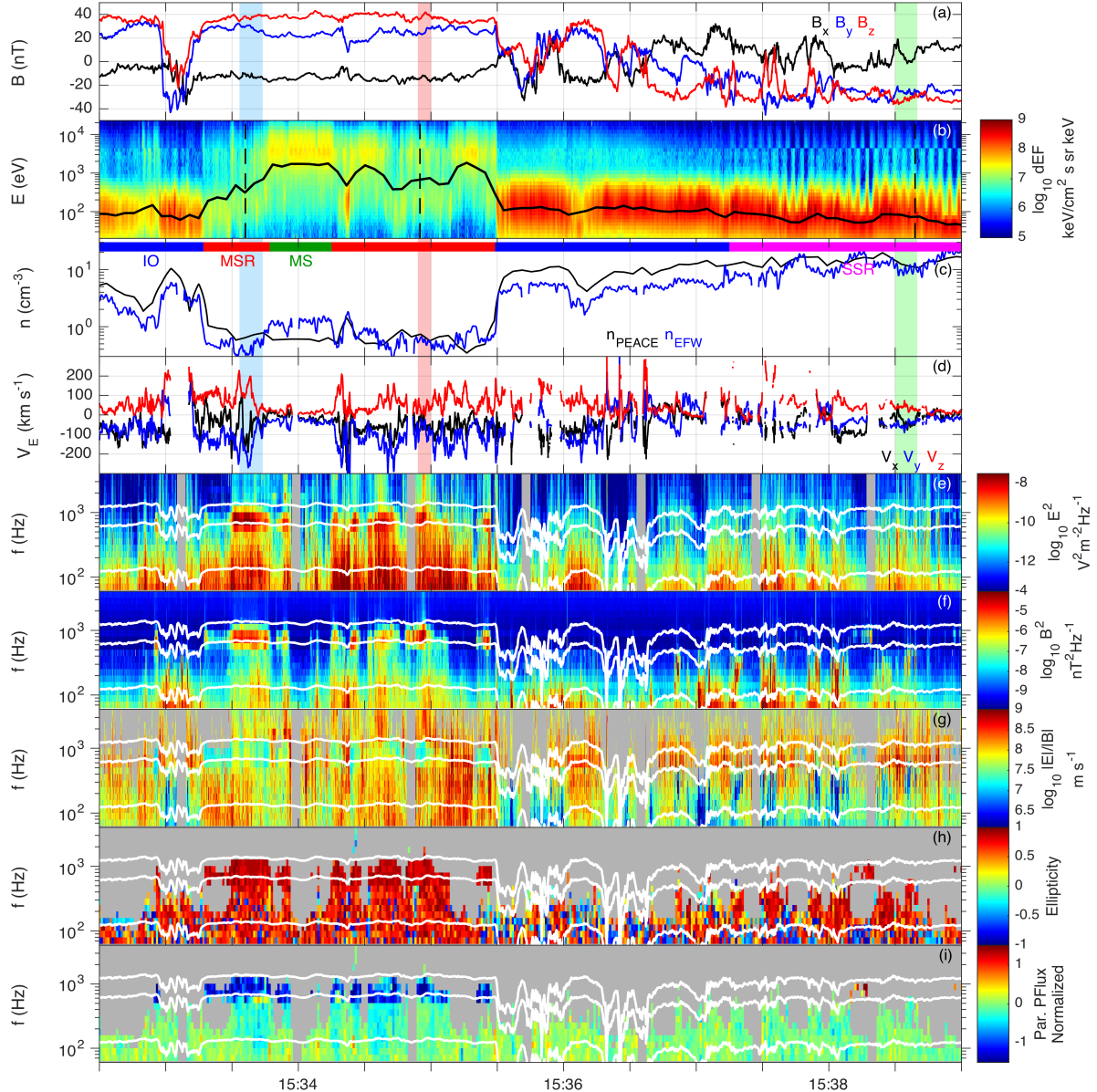


Figure 2. Magnetopause crossings observed by C2 on 17 April 2007. (a) \mathbf{B} (GSM). (b) Omnidirectional electron differential energy flux and T_e (black line). The vertical dotted lines indicate electron distributions investigated in Figure 4. (c) n_e obtained from PEACE and the spacecraft potential (EFW). The blue, red, green, and magenta horizontal bars indicate the ion outflow regions (IO), magnetosheath separatrix regions (MSR), magnetosphere (MS), and the magnetosheath separatrix region (SSR), respectively. (d) E-cross-B velocity \mathbf{V}_E (GSM). (e) and (f) \mathbf{E} and \mathbf{B} spectrograms. (g) Spectrogram of $\log_{10} |\mathbf{B}|$, which provides an estimate of the phase speed of whistlers. (h) Ellipticity (+1 indicates right-hand circular polarization and -1 indicates left-hand circular polarization). (i) Parallel Poynting vector normalized by its standard deviation. Positive values indicate propagation parallel to \mathbf{B} and negative values indicate antiparallel propagation. The white lines in panels (e)-(i) indicate the phase speed of whistlers. The vertical dotted lines in panel (b) indicate electron distributions investigated in Figure 4. The horizontal bars in panel (c) indicate regions: IO (blue), MSR (red), MS (green), and SSR (magenta). The white lines in panels (e)-(i) indicate the phase speed of whistlers.

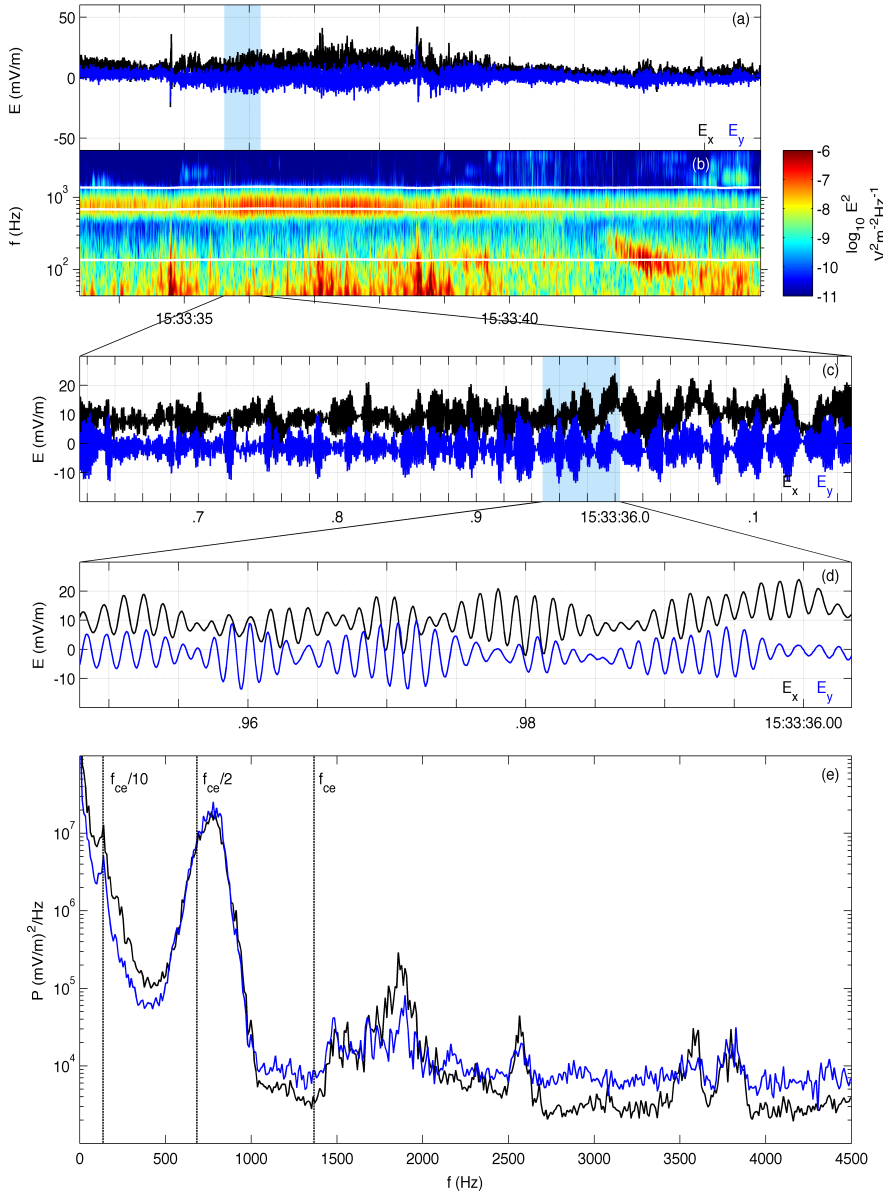


Figure 3. Electric field waveform recorded during EFW's internal burst mode (the blue shaded region in Figure 2). (a) Time series of E_x (black) and E_y (blue) in spacecraft (IRS2) coordinates and (b) the associated $|E|$ spectrogram (white lines are $0.1f_{ce}$, $0.5f_{ce}$, and f_{ce}). (c) and (d) Short time series of E_x and E_y . (e) Power spectra of E_x and E_y over the entire time series.

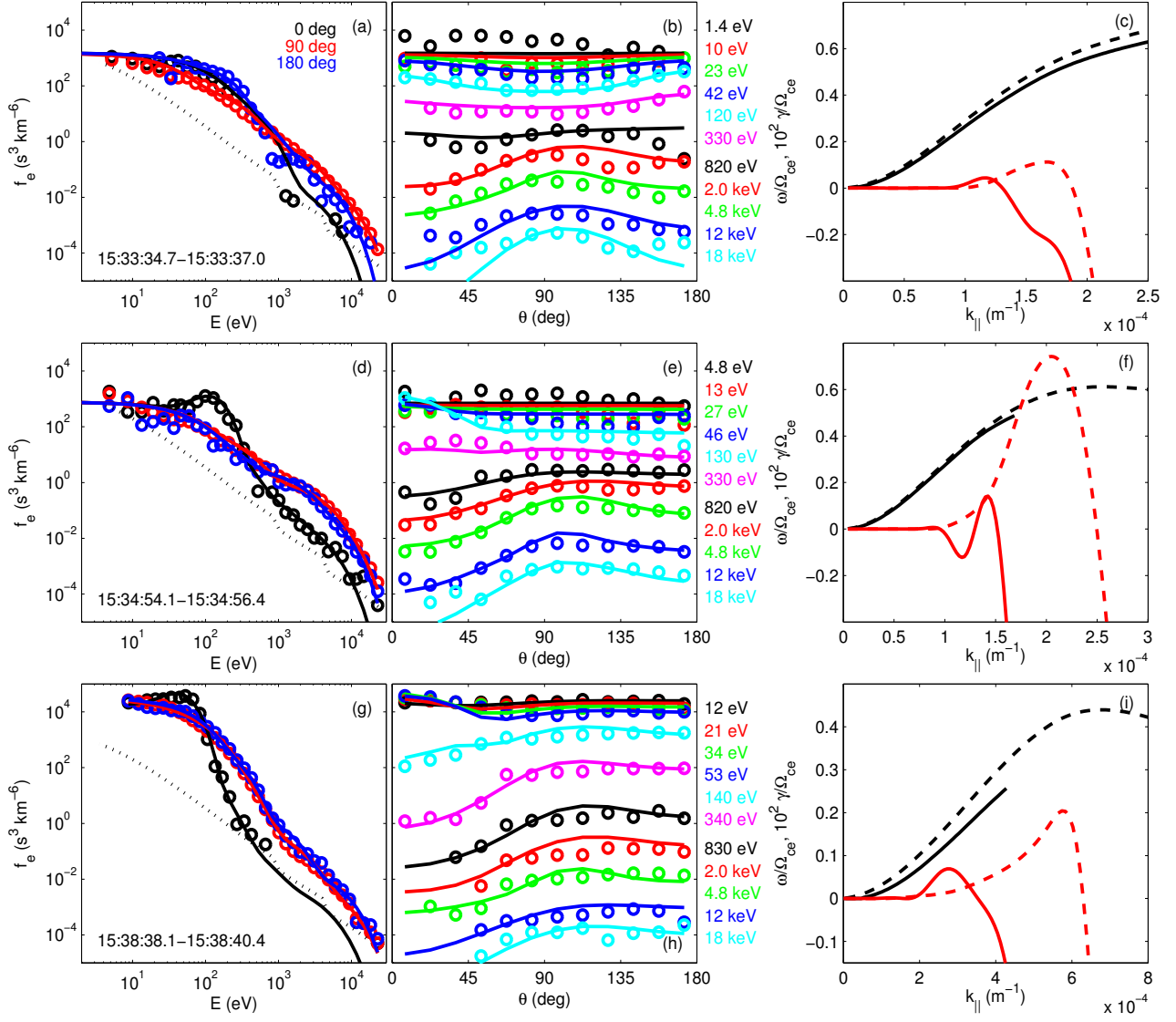


Figure 4. Observed and fitted $f_e(E)$ and the associated whistler modes predicted from the fitted distributions. (a), (d), and (g) $f_e(E)$ versus E at $\theta = 0^\circ$ (black), 90° (red), and 180° (blue). (b), (e), and (h) are $f_e(E)$ versus θ for constant E . The circles are observations and the lines are fits to the data. The dotted line is the instrumental one-count level. (c), (f), and (i) are the whistler modes predicted from the fitted $f_e(E)$. Black lines are the dispersion relations and the red lines are growth rates. Solid and dashed lines are the modes parallel and antiparallel to \mathbf{B} , respectively. From top to bottom the rows correspond to time intervals in the blue, red, and green intervals in Figure 2, respectively.

Table 2. Properties of the observed whistler waves and those predicted from linear theory.

Event	Observed				Linear theory			
	f (Hz)	k_{\parallel} (m $^{-1}$)	λ_{\parallel} (km)	v_{ph} (km s $^{-1}$)	f (Hz)	k_{\parallel} (m $^{-1}$)	λ_{\parallel} (km)	v_{ph} (km s $^{-1}$)
17 April 2007 (blue)	775	1.1×10^{-4}	54	4.3×10^4	740	1.7×10^{-4}	37	2.7×10^4
17 April 2007 (red)	800	2.5×10^{-4}	25	2.0×10^4	750	2.0×10^{-4}	31	2.4×10^4
17 April 2007 (green)	350	4.3×10^{-4}	15	5.1×10^3	470	5.7×10^{-4}	11	5.2×10^3
22 April 2008 (blue)	1100	4.1×10^{-4}	15	1.7×10^4	920	1.6×10^{-4}	39	3.6×10^4

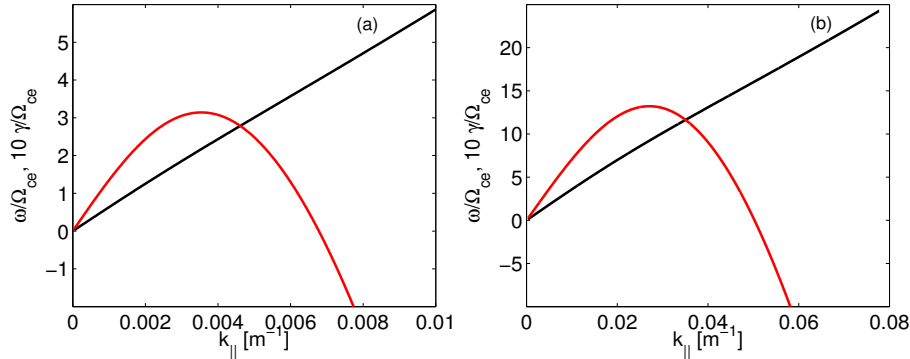


Figure 5. Beam mode dispersion relations for the electron distributions in (a) Figures 4d–4e and (b) Figures 4g–4h. The black lines are the dispersion relations and the red lines are the growth rates.

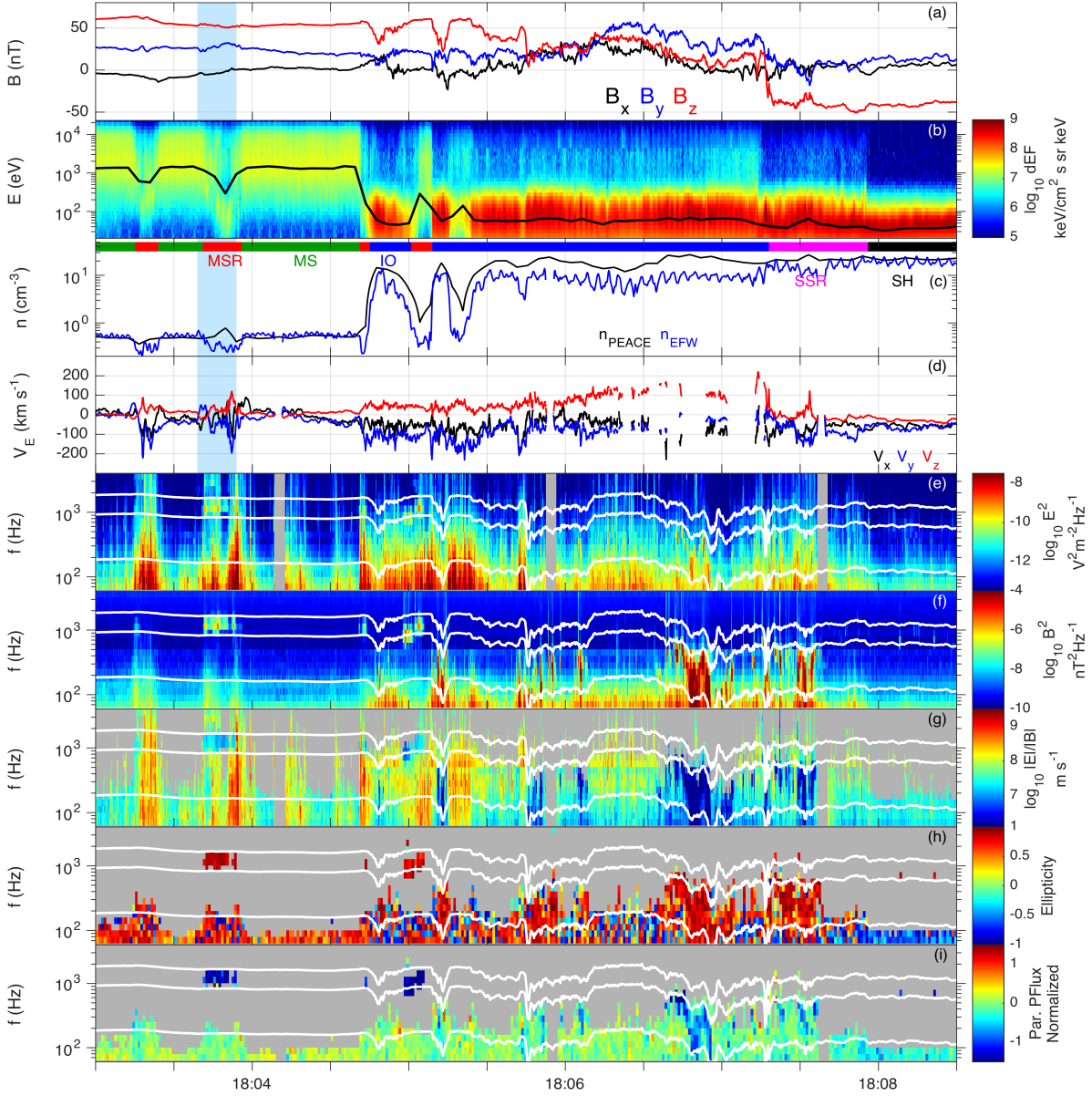


Figure 6. Magnetopause crossing observed by C2 on 22 April 2008. (a) \mathbf{B} (GSM). (b) Omnidirectional electron differential energy flux and T_e (black line). (c) n_e obtained from PEACE and the spacecraft potential (EFW). The blue, red, green, magenta, and black horizontal bars indicate the ion outflow regions (IO), magnetospheric separatrix regions (MSR), magnetosphere (MS), the magnetosheath separatrix region (SSR), and magnetosheath (SH) respectively. (d) E-cross-B velocity \mathbf{V}_E . (e) and (f) \mathbf{E} and \mathbf{B} spectrograms. (g) Spectrogram of $|\mathbf{E}|/|\mathbf{B}|$, which provides an estimate of the phase speed. Ph Real Ellipticity (+1 indicates right-hand circular polarization and -1 indicates left-hand circular polarization). (i) Parallel Poynting vector normalized by its standard deviation. The white lines in (e)–(i) are $0.1f_{ce}$, $0.5f_{ce}$, and f_{ce} .

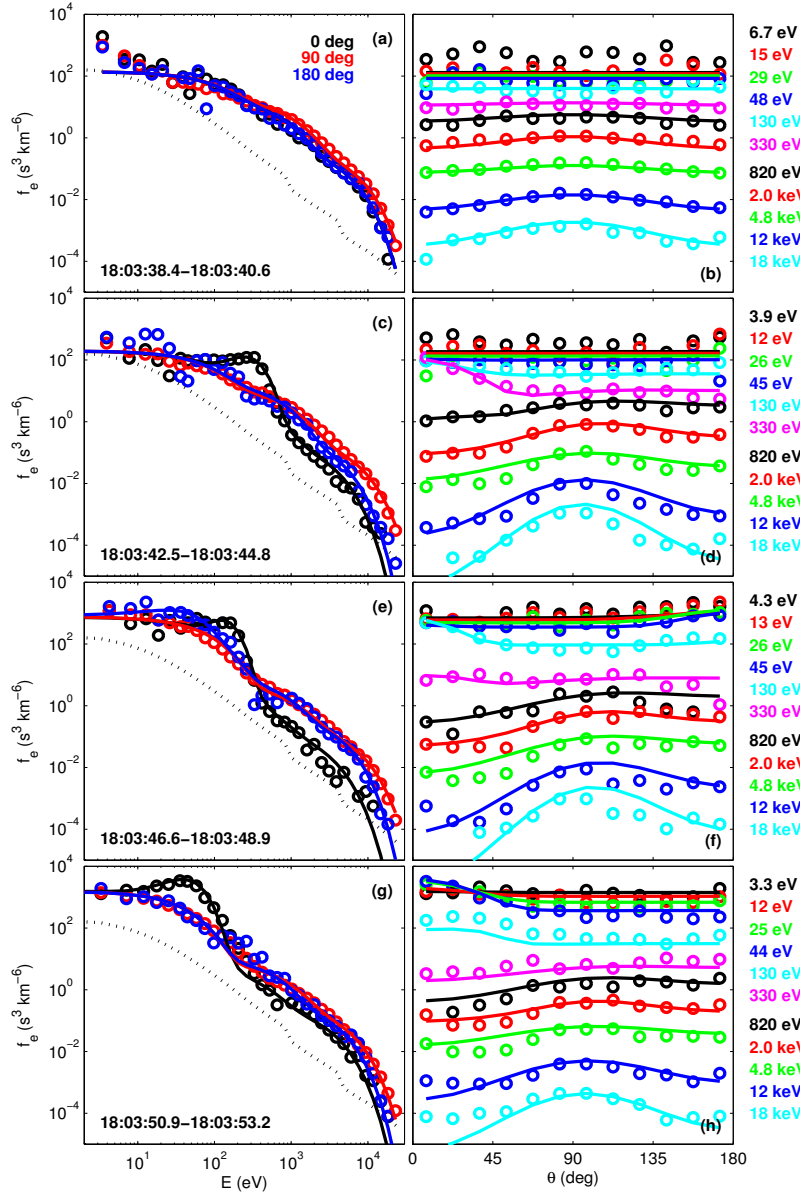


Figure 7. Observed and fitted $f_e(E)$ for the separatrix region observed between 18:03:38 UT and 18:03:54 UT on 22 April 2008 by C2. (a), (c), (e), and (g) $f_e(E)$ versus E for $\theta = 0^\circ$ (black), 90° (red), and 180° (blue). The dotted line is the instrumental one-count level. (b), (d), (f), and (h) $f_e(E)$ versus θ at constant E . In each panel the circles are the observed data and the lines are the fits. The observed times for each $f_e(E)$ are stated in the left panels.

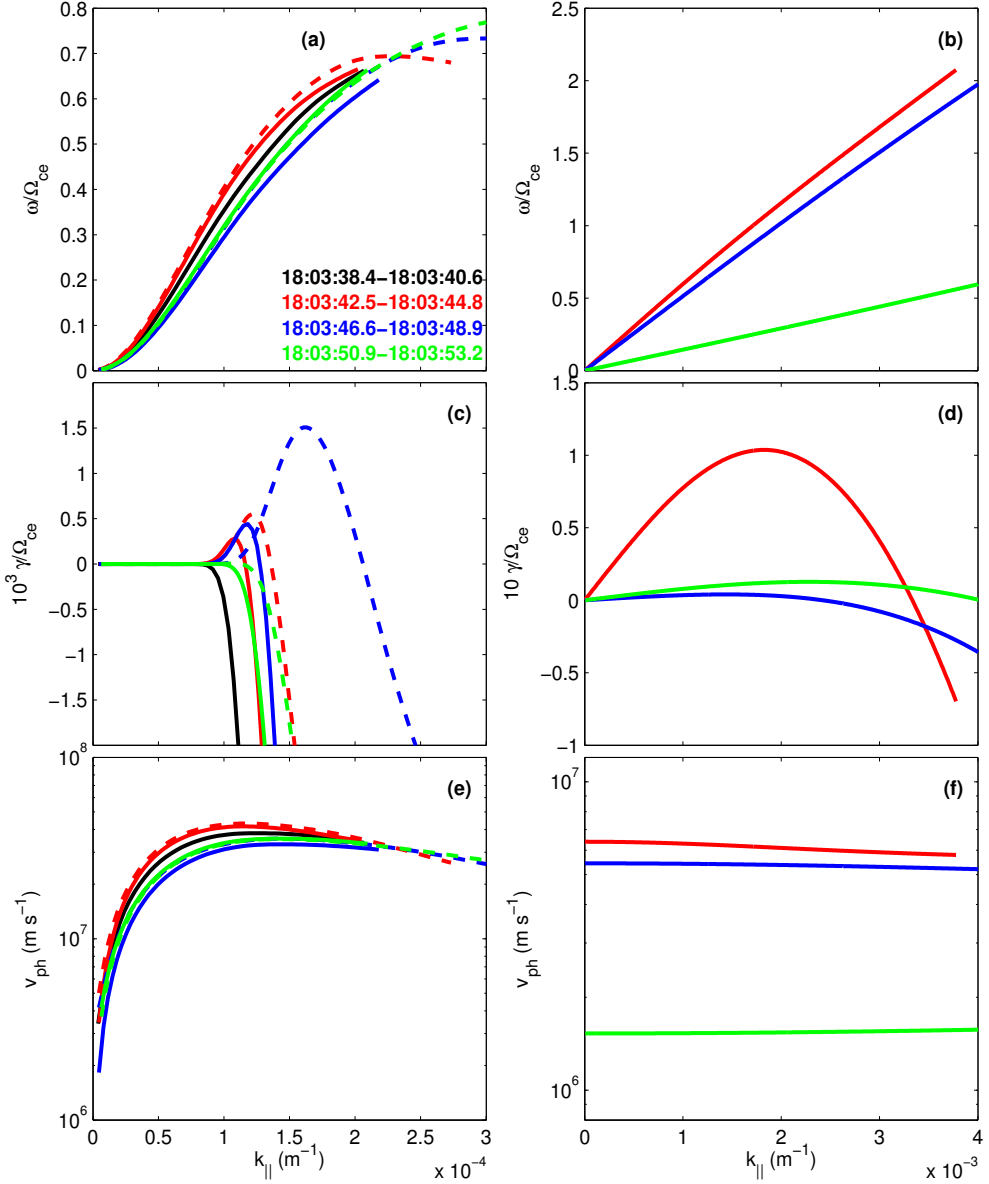


Figure 8. Whistler and beam mode solutions, left and right panels, respectively, for the distributions in Figure 7. (a) and (b) ω/Ω_{ce} versus k_{\parallel} . (c) and (d) γ/Ω_{ce} versus k_{\parallel} . (e) and (f) v_{ph} versus k_{\parallel} . Solid lines are modes with wave vectors parallel to \mathbf{B} and dashed lines are modes with wave vectors antiparallel to \mathbf{B} .

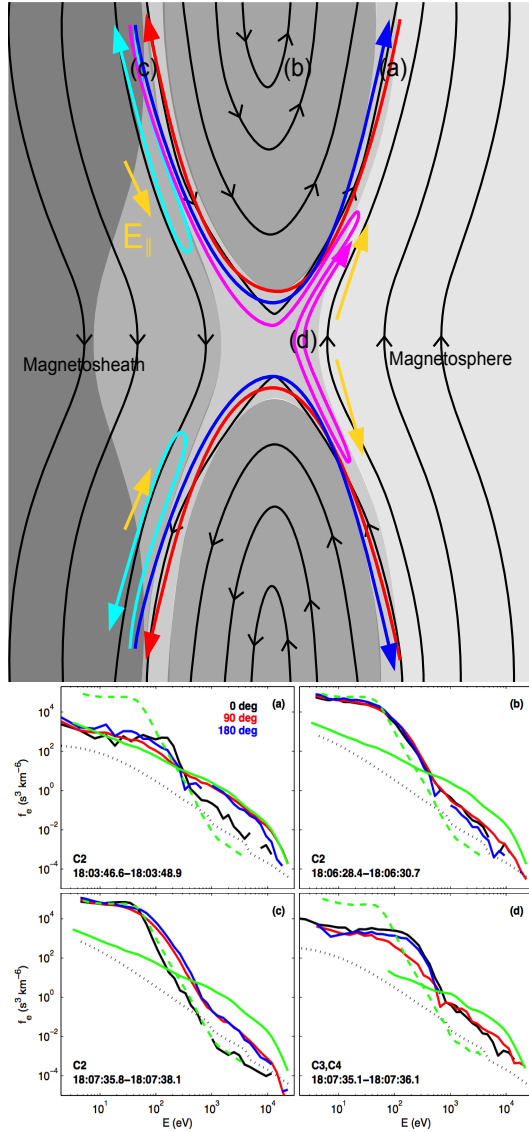


Figure 9. Diagram of asymmetric reconnection and associated $f_e(E)$. The top panel is a diagram of asymmetric reconnection showing \mathbf{B} (black lines), expected \mathbf{E}_{\parallel} (yellow arrows), and n_e (gray shading, with darker shading corresponding to higher n_e). Overplotted are the expected electron trajectories for reflected magnetosheath electrons (light blue), incoming magnetosheath electrons (dark blue), trapped magnetosheath electrons (magenta), and escaping magnetospheric electrons (red). Panels (a)–(d) show observed $f_e(E)$ for $\theta = 0^\circ$ (black), 90° (red), 180° (blue) in the magnetospheric separatrix region, outflow region, magnetosheath separatrix region, and ion diffusion region, respectively. Overplotted are the unperturbed angle-averaged magnetospheric and magnetosheath $f_e(E)$ (green and blue dashed lines, respectively).